The Astrophysical Journal, 835:77 (19pp), 2017 January 20 doi:10.3847/1538-4357/835/1/77

A NEW GENERATION OF PARSEC-COLIBRI STELLAR ISOCHRONES INCLUDING THE TP-AGB PHASE

Paola Marigo[1], Léo Girardi[2], Alessandro Bressan[3], Philip Rosenfield[4], Bernhard Aringer[1], Yang Chen[1], Marco Dussin[1], Ambra Nanni[1], Giada Pastorelli[1], Thaíse S. Rodrigues[1,2], Michele Trabucchi[1], Sara Bladh[1], Julianne Dalcanton[5], Martin A. T. Groenewegen[6], Josefina Montalbán[1], and Peter R. Wood[7]
[1] Dipartimento di Fisica e Astronomia Galileo Galilei, Università di Padova, Vicolo dell'Osservatorio 3, I-35122 Padova, Italy
[2] Osservatorio Astronomico di Padova—INAF, Vicolo dell'Osservatorio 5, I-35122 Padova, Italy
[3] SISSA, via Bonomea 365, I-34136 Trieste, Italy
[4] Harvard-Smithsonian Center for Astrophysics, 60 Garden Street, Cambridge, MA 02138, USA
[5] Department of Astronomy, University of Washington, Box 351580, Seattle, WA 98195, USA
[6] Koninklijke Sterrenwacht van België, Ringlaan 3, B-1180 Brussels, Belgium
[7] Research School of Astronomy and Astrophysics, Australian National University, Cotter Road, Weston Creek, ACT 2611, Australia
Received 2016 June 21; revised 2016 November 7; accepted 2016 November 14; published 2017 January 19

ABSTRACT

We introduce a new generation of PARSEC–COLIBRI stellar isochrones that includes a detailed treatment of the thermally pulsing asymptotic giant branch (TP-AGB) phase, covering a wide range of initial metallicities ($0.0001 < Z_i < 0.06$). Compared to previous releases, the main novelties and improvements are use of new TP-AGB tracks and related atmosphere models and spectra for M and C-type stars; inclusion of the surface H+He +CNO abundances in the isochrone tables, accounting for the effects of diffusion, dredge-up episodes and hot-bottom burning; inclusion of complete thermal pulse cycles, with a complete description of the in-cycle changes in the stellar parameters; new pulsation models to describe the long-period variability in the fundamental and first-overtone modes; and new dust models that follow the growth of the grains during the AGB evolution, in combination with radiative transfer calculations for the reprocessing of the photospheric emission. Overall, these improvements are expected to lead to a more consistent and detailed description of properties of TP-AGB stars expected in resolved stellar populations, especially in regard to their mean photometric properties from optical to mid-infrared wavelengths. We illustrate the expected numbers of TP-AGB stars of different types in stellar populations covering a wide range of ages and initial metallicities, providing further details on the "C-star island" that appears at intermediate values of age and metallicity, and about the AGB-boosting effect that occurs at ages close to 1.6-Gyr for populations of all metallicities. The isochrones are available through a new dedicated web server.

Key words: stars: abundances – stars: AGB and post-AGB – stars: carbon – stars: evolution – stars: general – stars: mass loss

1. INTRODUCTION

Theoretical stellar isochrones are remarkably useful data sets in astrophysics. Historically, they have been commonly used to attribute approximated ages and distances to star clusters observed in at least two filters, in the traditional process of isochrone fitting (since, e.g., Demarque & McClure 1977). In the last decades, their use has expanded in many different ways. Since Charlot & Bruzual (1991), they have been considered the basis of the isochrone method of the spectro-photometric evolutionary population synthesis, which has revolutionized the interpretation of the spectra and photometry of distant galaxies. They have also been extensively used in the more complex methods of CMD fitting of nearby galaxies and star clusters (e.g., Dolphin 2002), which aim at deriving quantitative measurements of their star formation and chemical enrichment histories.

While the most traditional applications of isochrones refer to the interpretation of spectrophotometric data only, more recent applications regard other quantities as well. For instance, the advent of large microlensing (Paczynski 1996) and spectroscopic surveys (York et al. 2000) in the nineties has opened access to the variability and the chemical composition information for huge populations of stars in the Milky Way and its satellite galaxies, while the onset of space-based asteroseismology now gives access to fundamental quantities such as the masses and radii even for stars located tens of kiloparsecs away (Chaplin & Miglio 2013). The interpretation of such data in terms of stellar populations and ages requires that, besides the photometry, additional intrinsic stellar properties are provided along the isochrones.

This need for more information is particularly important when we refer to thermally pulsing asymptotic giant branch (TP-AGB) stars. They contribute to a sizable fraction of the integrated light of stellar populations, and are responsible for a significant fraction of the chemical enrichment and dust production in galaxies. Yet, the TP-AGB phase is still the most uncertain among the main evolutionary phases of single stars, since its evolution is determined by a series of complex and interconnected processes that still cannot be simply modeled from first principles—like the third dredge-up episodes, long-period pulsation and mass loss, and so on (see Frost & Lattanzio 1996; Mowlavi 1999; Herwig 2005; Marigo 2015). The calibration of this phase *requires* the construction of extended sets of isochrones in which all the relevant processes are considered and all the relevant observables are tabulated. Only in this way we can enable a quantitative comparison between the model predictions and the properties of TP-AGB populations observed in nearby galaxies.

Indeed, in Marigo et al. (2008) we made a significant step in this direction, by providing the first isochrones in which the properties of TP-AGB stars were considered in more detail, and

including crucial processes like third dredge-up, hot-bottom burning, low-temperature opacity changes, the distinct spectra of carbon (C) stars, the reprocessing of radiation by circumstellar dust in phases of increased mass loss, and the expected pulsation periods. In this paper, we provide new isochrones derived from the stellar evolutionary tracks computed with the more recent PARSEC (Bressan et al. 2012) and COLIBRI (Marigo et al. 2013) codes. They include more details than the previous isochrones, and are specifically designed to allow us to advance in the process of calibration of the TP-AGB evolution. Some aspects of these isochrones, such as the inclusion of chemical abundance information, will be of interest to many other isochrone users as well. The input data and methods are described in Section 2. Some new properties of the new isochrones are illustrated in Section 3. Data retrieval and ongoing work are briefly described in Section 4.

2. DATA AND METHODS

2.1. PARSEC Tracks

PARSEC (the Padova and Trieste Stellar Evolutionary Code) represents a deeply revised version of the Padova code used in many popular sets of isochrones (e.g., in Bertelli et al. 1994; Girardi et al. 2000, 2010; Marigo et al. 2008). The main features in PARSEC are described in Bressan et al. (2012, 2013), and include the updating of the input physics (equation of state, opacities, nuclear reaction rates, solar reference abundances) and of mixing processes, in particular with the addition of microscopic diffusion in low-mass stars. Further updates regard the treatment of boundary conditions in low-mass stars (Chen et al. 2014), and envelope overshooting and mass loss in intermediate- and high-mass stars (Tang et al. 2014; Chen et al. 2015). As it is clear from these papers, PARSEC is a rapidly evolving code, with further revisions underway.

In the present work, we use a subset of the PARSEC V1.2S evolutionary tracks as a reference. They include grids of tracks for 15 values of initial metal content, $Z_{\rm i}$, between 0.0001 and 0.06. The helium initial content, $Y_{\rm i}$, follows the initial metal content according to the $Y_{\rm i} = 1.78 \times Z_{\rm i} + 0.2485$ relation, so as to reproduce both the primordial Y value by Komatsu et al. (2011) and the chemical composition of the present Sun (namely, $Z_\odot = 0.01524$, $Y_\odot = 0.2485$; see Bressan et al. 2013 for details). The reference solar-scaled composition is taken from Caffau et al. (2011). Adopting the simple approximation of $[{\rm M/H}] = \log(Z_{\rm i}/Z_\odot) - \log(X_{\rm i}/X_\odot)$, the metallicity [M/H] ranges from -2.19 to $+0.70$ dex.

The range of masses computed with PARSEC is also very wide, generally including $\sim$120 different mass values distributed in the range from 0.1 to 350 $M_\odot$ for each metallicity. The mass range more relevant for this paper is the one from $\sim$0.5 $M_\odot$ up to the maximum mass of stars developing the TP-AGB phase, which is located somewhere between 5 and 6.4 $M_\odot$, depending on metallicity. This mass–metallicity range is presented in Figure 1, together with a summary of the evolutionary phases computed in every case.

2.2. COLIBRI Tracks

The TP-AGB evolutionary tracks from the first thermal pulse up to the complete ejection of the envelope are computed with the COLIBRI code developed by Marigo et al. (2013), and including the updates in the mass loss described by Rosenfield et al. (2014, 2016). While many details of COLIBRI are described in the aforementioned works, let us highlight here the main differences with respect to the previous TP-AGB tracks computed by Marigo & Girardi (2007), which were used in the stellar isochrones of Marigo et al. (2008). We recall that COLIBRI couples a synthetic module (which contains the main free parameters to be calibrated) with the numerical solution of the atmosphere and complete envelope model, down to the bottom of the H-burning shell. The integration strategy is detailed Marigo et al. (2013), where several accuracy tests with respect to full stellar models are also presented. COLIBRI is characterized by a high computational speed and a robust numerical stability, allowing us to promptly compute large sets of TP-AGB tracks any time we aim at exploring the impact of a different model prescription. Such a feature is really essential to perform the demanding TP-AGB calibration cycle. At the same time, COLIBRI incorporates many revisions in the input physics, some of which (e.g., the nuclear reaction rates) are also common to PARSEC. More importantly, COLIBRI is the first code to fully include the on-the-fly computation of the equation of state and Rosseland mean opacities by suitably calling, at each time step, the Opacity Project routines (for $T > 12.000$ K; Seaton 2005), and the ÆSOPUS routines (for $1.500 \leqslant T \leqslant 12.000$ K; Marigo & Aringer 2009) in full consistency with the actual composition of the stellar envelope. Therefore, composition-changing processes such as the third dredge-up (3DU) and the hot-bottom burning (HBB) at the base of the convective envelope produce an immediate effect in the stellar structure and on stellar properties such as the effective temperature, $T_{\rm eff}$, hence also changing the efficiency of other processes such as the mass loss rate, $\dot{M}$; pulsation periods; and so on. Similar effects of feedback between chemical composition and stellar structure were also included in Marigo & Girardi (2007) models, but in a much simpler way (see Marigo 2002). Moreover, COLIBRI improves in the description of other effects, such as the stellar sphericity and the integration of extended nuclear networks for all burning processes—including the HBB, which requires a detailed consideration of both nuclear and convective time scales.

The occurrence and efficiency of the 3DU process in TP-AGB stars is notoriously uncertain and sensitive to numerical details (Frost & Lattanzio 1996; Mowlavi 1999). As in Marigo & Girardi (2007) models, this process is parameterized also in COLIBRI. This causes the model to have a few efficiency parameters (for 3DU and mass loss) that can be tuned so as to reproduce the observed properties of populations of AGB stars.

The COLIBRI models illustrated in this work are the same ones as described in Rosenfield et al. (2016), which are shown to reproduce the AGB star numbers in a set of nearby dwarf galaxies. They include the complete range of masses and metallicities required to complement the PARSEC V1.2S grid of tracks, as shown in Figure 1. About 60 TP-AGB tracks are computed for each metallicity. The initial conditions of every COLIBRI track (core mass, luminosity, envelope composition, etc.) are taken from the corresponding PARSEC track just before the first significant thermal pulse; therefore the subsequent section of the PARSEC track is simply replaced by the COLIBRI one. As illustrated by Marigo et al. (2013), this gives origin to an almost continuous track, with just a small jump in the $T_{\rm eff}$ (typically less that 50 K; see their Figure 6) at the PARSEC–COLIBRI junction.

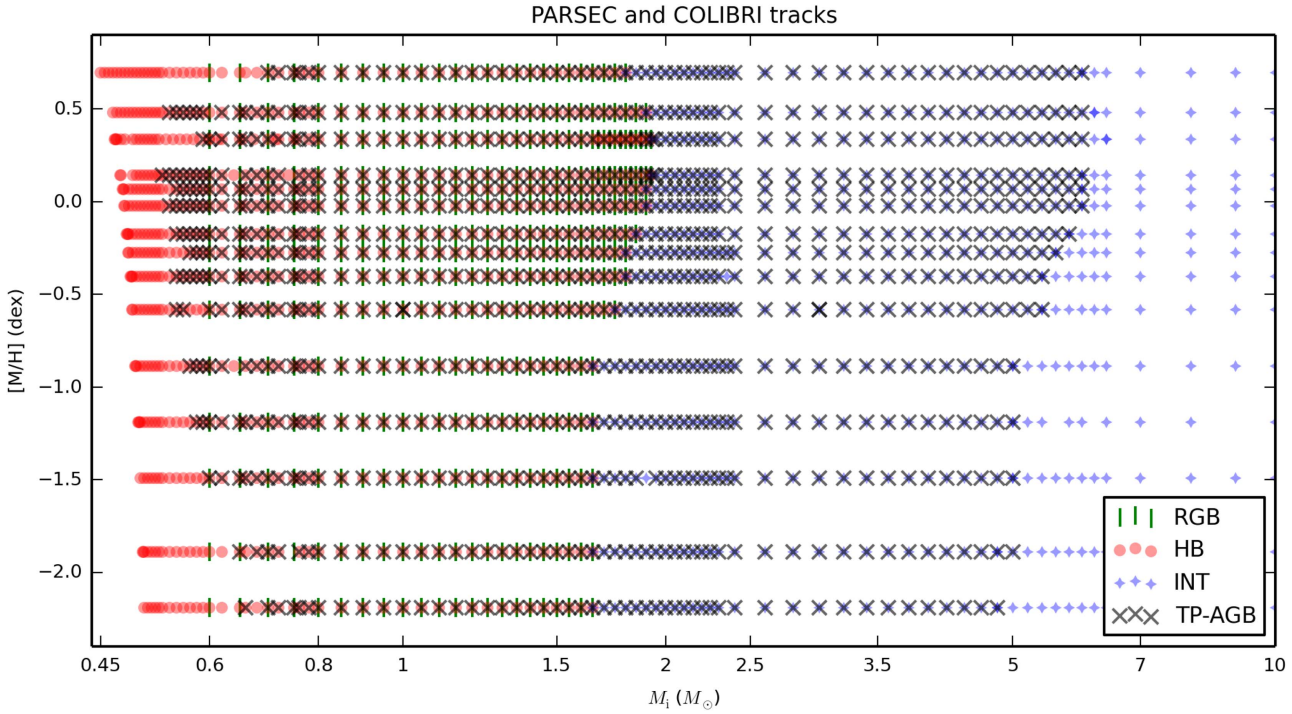

Figure 1. The set of tracks involved in the construction of PARSEC-COLIBRI isochrones, in the [M/H] vs. M_i plane. Tracks from PARSEC are divided into three broad classes tagged as RGB (low-mass tracks from the pre-MS up to the He-flash at the tip of the RGB), HB (low-mass tracks from the start of quiescent core He-burning up to the first TPC on the TP-AGB), and INT (intermediate-mass and massive tracks from the pre-MS up to either a first TPC or C ignition). For all cases where a first TPC was detected, the TP-AGB evolution (as tagged) was followed with the COLIBRI code. In addition to the tracks presented here, the PARSEC database includes very low-mass tracks, down to 0.1 $M_\odot$ and evolved up to an age larger than the Hubble time, and massive tracks up to 350 $M_\odot$ and evolved up to C ignition; they are not shown in the plot but are also included in the available isochrones.

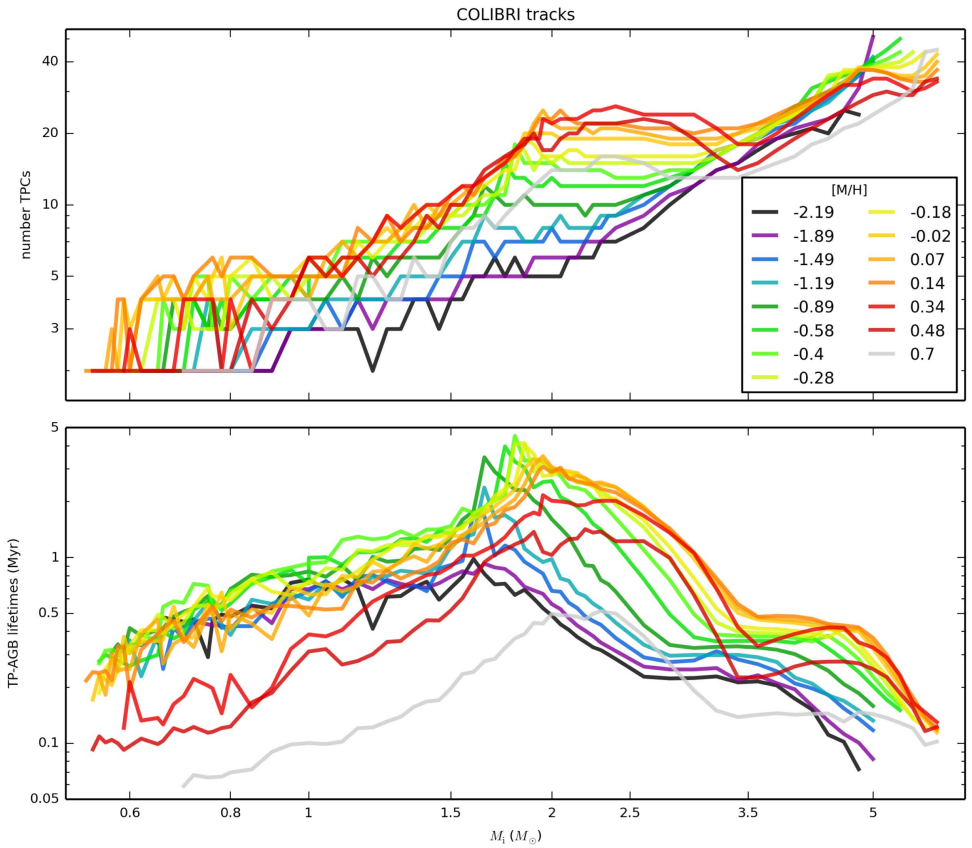

Figure 2. Number of TPCs in every COLIBRI TP-AGB track (top panel), and its total lifetime (bottom panel).

Figure 2 shows two of the basic properties of these tracks, namely the number of TPCs and the total TP-AGB lifetime, as a function of initial mass and metallicity.

2.3. Equivalent Evolutionary Points and Interpolation Method

The grids of stellar evolutionary tracks describe how the stellar properties—here generically denoted by p—vary as a function of stellar age, t, for a given set of initial masses, $M_{\rm i}$. Building isochrones is essentially the process of interpolating inside this grid to produce a sequence of such properties as a function of $M_{\rm i}$ for a given set of t, that is,

$$\boxed{\begin{array}{c}\text{Tracks}\\ p(t)|_{M_{\rm i}=\text{const.}}\end{array}} \Rightarrow \boxed{\begin{array}{c}\text{Isochrones}\\ p(M_{\rm i})|_{t=\text{const.}}\end{array}}. \quad (1)$$

In order to do this, we employ the classic method of interpolating between tracks using pairs of equivalent evolutionary points (EEP) as a reference. Essentially, once a pair of EEPs is identified in two adjacent tracks, the whole evolutionary sequence between these EEPs is assumed to be equivalent and interpolated in all quantities, by using $M_{\rm i}$ and age as the independent variables. After building a dense grid of interpolated tracks of masses $M_{\rm i}$, the simple selection of points with desired age t allows us to draw a complete isochrone. Moreover, by following an algorithm similar to Bertelli et al. (2008), the available grids of tracks are also interpolated for any intermediate value of initial metallicity. Tracks that share similar evolutionary properties—e.g., tracks with an extended red giant branch (RGB), or tracks with a convective core on the main sequence—are grouped together and have their EEPs selected with exactly the same criteria, so that the interpolations turn out to be smooth not only as a function of initial mass and age, but also as a function of metallicity.

According to this scheme, the interpolated tracks can be built with any arbitrary density in initial mass coordinate; the higher the density, the larger the number of points in the resulting isochrones. In order to limit these numbers, we use a dynamical interpolation algorithm that, for every track section being considered, creates as many interpolated tracks (and hence isochrone points) as necessary to obtain a given resolution in the $\log L$ versus $\log T_{\rm eff}$ space. In the present release, this resolution is set to a minimum of $\Delta \log L = 0.04$ dex and $\Delta \log T_{\rm eff} = 0.01$ dex, for all sections of PARSEC tracks; this results in isochrones containing a few hundred points before the first TPC. The TP-AGB resolution is defined in a different way, as we specify in the following discussion.

The algorithm we developed to build the isochrones is very general, even allowing us to identify the presence of multiple sequences of evolutionary stages along the same isochrone, as those illustrated in Girardi et al. (2013); more specifically, in that work we have identified the presence of double or triple TP-AGB sequences causing a marked "AGB-boosting" effect in isochrones (and star clusters) of ages close to 1.6 Gyr.

2.4. Mass Loss on the RGB

Another important detail is that we can apply a modest amount of mass loss between the tip of the RGB and the zero-age core-helium burning (CHeB) stage of low-mass stars, in order to simulate the effect of mass loss along the RGB. Just as in previous releases (Girardi et al. 2000; Marigo et al. 2008), this is done in an approximative way: we first estimate the amount of mass loss expected from a given mass loss formula, ΔM, by integrating the mass loss rate along the RGB section of the evolutionary tracks (i.e., $\Delta M = \int_{\rm RGB} \dot{M} dt$). Then the function $\Delta M(M_{\rm i})$ is used to assign every RGB track of mass $M_{\rm i}$ to a given CHeB+AGB evolutionary sequence of mass $M_{\rm i} - \Delta M(M_{\rm i})$. The CHeB+AGB sequence is created by interpolation in the existing grid, and then attached to the RGB track while ensuring the continuity of the stellar age along the entire sequence. The modified RGB+CHeB+AGB tracks are then used to build the isochrones. This is a realistic approximation for low-mass stars, in which the RGB mass loss affects neither the evolution of the stellar core nor the shape of evolutionary tracks in a significant way.

By default, we apply the classical Reimers's (1975) mass loss formula with a multiplicative coefficient of $\eta_{\rm R} = 0.2$ (Miglio et al. 2012), for stars of masses smaller than 1 $M_\odot$. Then an additional multiplicative factor is assumed in order to decrease the mass loss predicted by this formula gradually as the initial mass increases from 1.0 to 1.7 $M_\odot$. In this way, stars of masses $M_{\rm i} \gtrsim 1.5\ M_\odot$, for which the present algorithm might provide inconsistent results, are little affected by mass loss. Stars of masses $M_{\rm i} \gtrsim 1.7\ M_\odot$ are assumed not to lose mass before the TP-AGB.

2.5. Thermal Pulse Cycle (TPC) L Variations

TPC L and $T_{\rm eff}$ variations are a basic feature of TP-AGB evolutionary tracks. They are quasi-periodic changes in L and $T_{\rm eff}$ caused by the onset of He-shell flashes and the subsequent cycle of envelope expansion, switching off of the He-shell, contraction, and gradual expansion as the quiescent H-shell burning takes over (see, e.g., Boothroyd & Sackmann 1988; Vassiliadis & Wood 1993; Wagenhuber & Groenewegen 1998). These basic features of the tracks, however, are very hard to obtain in the isochrones. The main problem is that the number of TPCs in general varies from track to track, even if they are separated by small intervals of initial mass and metallicity (e.g., 0.05 $M_\odot$ and 0.1 dex, respectively). This variation can be appreciated in the top panel of Figure 2.

Because the numbers of TPC are different, it is practically impossible to obtain TPC-looking features from the direct interpolation between adjacent TP-AGB evolutionary tracks. A typical situation is illustrated in panel (a) of Figure 3, where COLIBRI tracks of masses 1.60 and 1.65 $M_\odot$, and $Z_{\rm i} = 0.001$, are plotted in absolute age versus $\log L/L_\odot$. Although the tracks look similar in slope and span comparable age and $\log L/L_\odot$ intervals, the 1.65 $M_\odot$ track has nine TPCs (out of which, only eight are really complete), whereas the 1.60 $M_\odot$ has 7 TPCs.

To solve this problem, we apply a scheme that was devised during the first implementation of TP-AGB tracks in the population synthesis code TRILEGAL (Girardi & Marigo 2007): First, the complex TP-AGB tracks from COLIBRI are converted into simplified ones containing just the pre-flash quiescent stages.[8] A couple of such simplified tracks are illustrated in Figure 3(b). They look much smoother than the original tracks, and it is easy to make interpolations along them to derive versions containing more or less evolutionary points. In the illustrative case of Figure 3(b), we have generated simplified tracks containing six equally lasting TP-AGB

[8] Pre-flash quiescent stages are those in which the H-burning shell provides most of the stellar luminosity, immediately prior the ignition of the He-shell in a flash; see Wagenhuber & Groenewegen (1998) for a precise definition.

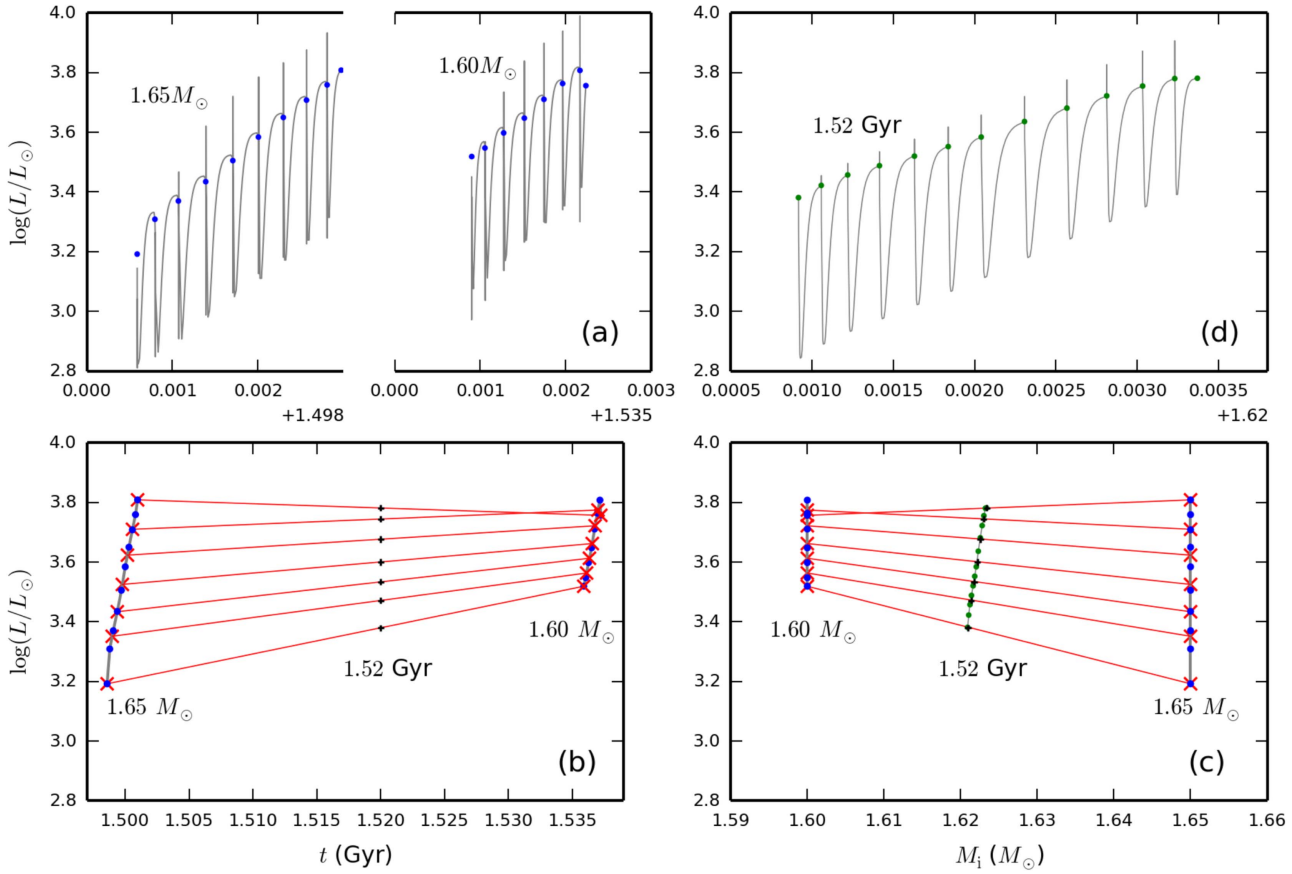

Figure 3. The sequence of operations involved in building a TP-AGB section of the isochrones, limited to the stellar property $\log L$ only. Left panels refer to evolutionary tracks, while right panels refer to the derived isochrones. The split panel (a) shows a couple of COLIBRI tracks of the same metallicity and close in initial mass (with $M_i = 1.65$ and 1.60 $M_\odot$, from left to right), in the absolute age t vs. $\log L$ plot. The continuous gray lines are the detailed TP-AGB evolution produced by COLIBRI, whereas the blue dots mark the pre-flash quiescent stages, or L_q. Panel (b) shows the same two tracks in a much simplified way, containing just the pre-flash quiescent stages. They draw simple sequences in the t vs. $\log L$ plane, which can be easily split into a series of equivalent sections, as illustrated in this case by splitting each track into six sections of equal Δt (delimited by the red crosses). Linear interpolations among these couple of equivalent points allow us to derive the $\log L$ for any arbitrary mass or age located between these tracks, as illustrated here by producing a series of intermediate points at a fixed age of 1.52 Gyr (black plus signs). Panel (c) shows the same situation as panel (b), but now in the M_i vs. $\log L$ plane, showing the initial mass M_i of every point produced at an age of 1.52 Gyr; they define a TP-AGB isochrone section containing only quiescent stages. The plot shows a few additional green points, which represent the somewhat denser grid of interpolated quiescent stages that is produced, by default, by our code. Panel (d) shows the final 1.52 Gyr isochrone in detail, after the detailed TPCs are re-introduced between the quiescent TP-AGB stages.

sections. This number of sub-intervals can be set at any arbitrary value; in general, however, we set it as equal to the maximum number of TPCs found in the mass interval being taken into consideration.

Quantities between these simplified tracks are interpolated using the same EEP scheme used for the pre-TP-AGB tracks; since they draw smooth lines in the Hertzsprung–Russell (HR) diagram, the derived isochrone sections will also contain a smooth and well-behaved sequence of quiescent pre-flash stages, as can be seen in the interpolated isochrone section of Figure 3(c).

In addition to L, other quantities characterizing the quiescent stages are stored and interpolated while creating the TP-AGB isochrone sections: they include $T_{\rm eff}$, the core mass $M_{\rm core}$, and the surface chemical composition. These quantities suffice to describe the complete luminosity profile $L(\phi)/L_q$ as a function of the phase during the TPC, ϕ, normalized to the pre-flash luminosity maximum L_q, using the formulas provided by Wagenhuber (1996) and Wagenhuber & Groenewegen (1998; just as done in COLIBRI by Marigo et al. 2013). Therefore, we first produce the isochrone TP-AGB sections containing just the quiescent luminosities (Figure 3(c)), and then we insert a number of points $n_{\rm inTPC}$ between them, following the detailed TPC luminosity evolution. This last step is illustrated in Figure 3(d). In this example we have adopted $n_{\rm inTPC} = 15$, which suffices to recover the main details of the TPCs. Thanks to our choices for the number of age intervals in the simplified TP-AGB tracks, the number of quiescent points on every isochrone (and hence of TPCs being inserted) turns out similar to the number found in the track with a mass equal to the turn-off one.

At this point, we have isochrones with detailed L variations along the TPCs, $\Delta \log L$, as further illustrated in the upper panels of Figure 4 for two particular isochrone sections: one intermediate-age isochrone at around the point in which third dredge-up drives the transition between O-rich and C-rich phases, and a young isochrone at around the point in which mass loss weakens the effect of HBB, allowing the same transition to occur. The remarkable difference in the TPC shape between these cases is caused mainly by their very different core and envelope masses.

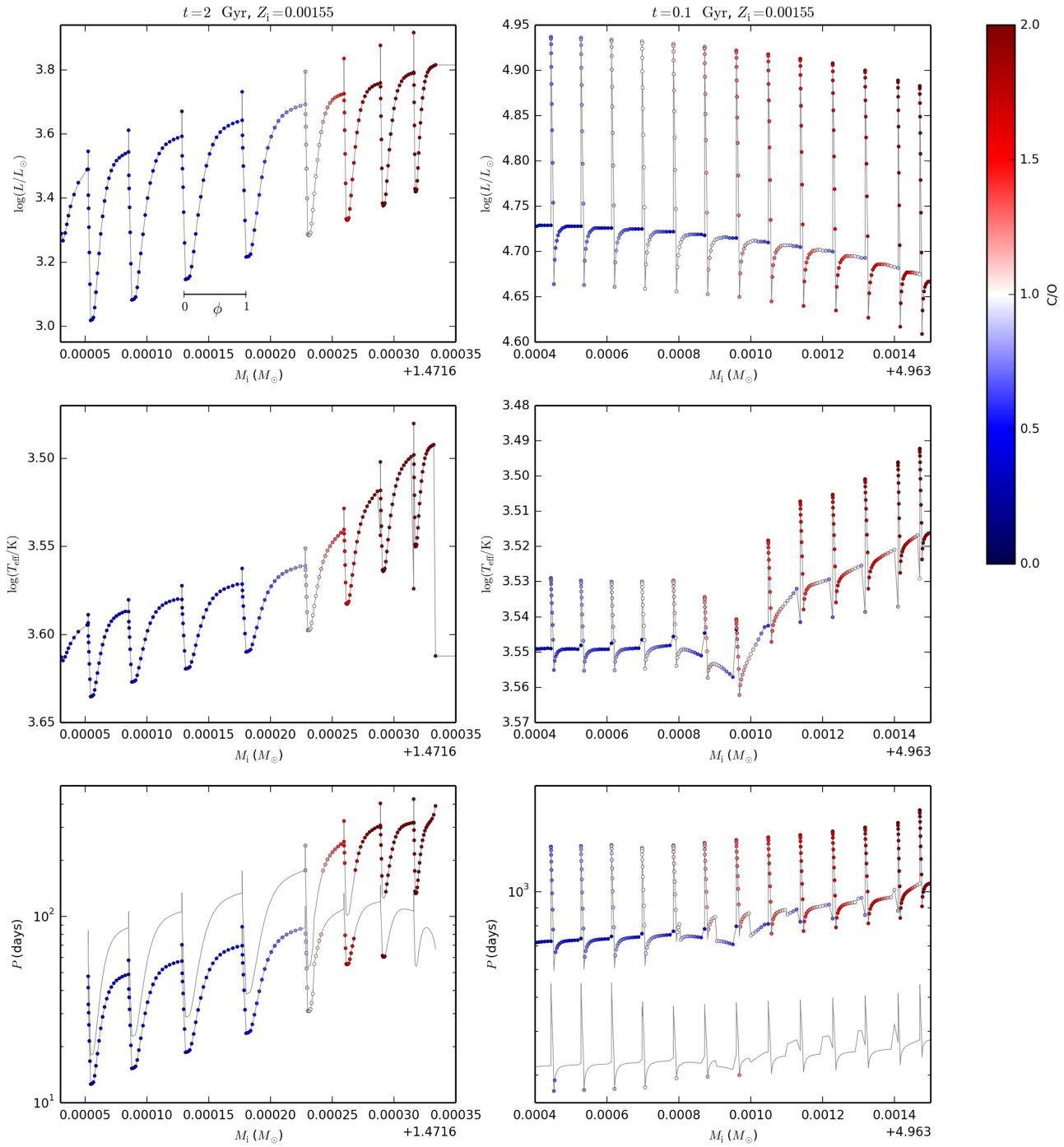

Figure 4. Examples of isochrones, zooming in on a few of their TPCs in the $\log L$, $\log T_{\rm eff}$, and period vs. $M_{\rm i}$ plots (from top to bottom). In the top and middle panels, the dots along the isochrones are those derived for $n_{\rm inTPC} = 25$. The inset axis illustrates the variation of phase ϕ along one of the inserted TPCs. The left panels show the complete TP-AGB section of an intermediate-age isochrone, where third dredge-up is operating and the C/O ratio steadily increases with $M_{\rm i}$. This isochrone describes the sequence from M to S to C-type stars (i.e., from C/O $<$ 1 to C/O $\sim$ 1 to C/O $>$ 1; see the color scale). The right panels show a much younger isochrone, where HBB is operating in addition to the third dredge-up. In this case HBB becomes gradually weaker for stars of higher $M_{\rm i}$, since they correspond to stars in more advanced stages of the TP-AGB, in which there is a significant reduction of the envelope (and total) masses. This situation results in the sequence from M to S to C types to occurring in reverse order inside individual TPCs. Finally, the bottom panels show the variation of LPV periods along these isochrone sections, for the fundamental mode and first-overtone modes (the gray lines with longer and shorter periods, respectively). The colored dots in this case signal the expected dominant period.

2.6. Thermal Pulse Cycle $T_{\rm eff}$ Variations

With the L variations reconstructed, the next problem is to insert detailed $T_{\rm eff}$ variations in the isochrones. For most TPCs in the original set of COLIBRI tracks, these $T_{\rm eff}$ variations closely follow the L variations, as the star goes up and down along its Hayashi line in the HR diagram. Indeed, we verify that every single TPC develops along the lines of nearly constant slope $\Delta \log T_{\rm eff} / \Delta \log L$. We recall that this behavior is derived from detailed envelope integrations in COLIBRI, which take into account the opacity variations deriving from

changes in atomic and molecular concentrations. $\Delta \log T_{\rm eff}/\Delta \log L$ is generally well-behaved along the O-rich section of the TP-AGB tracks (depending primarily on the initial metallicity), but its value changes abruptly from about -0.12 to -0.16 whenever a transition between an O-rich and C-rich star occurs—following the large variations in molecular opacities in the stellar atmospheres (Marigo 2002). In addition to this general behavior, we have the changes in $T_{\rm eff}$ due to substantial mass loss occurring at the last TPCs, in which while the luminosity increases mildly, $T_{\rm eff}$ decreases dramatically due to large mass loss, thus reducing the envelope mass. Hence the star moves between Hayashi lines of different masses. In this case, it is not appropriate to model the $T_{\rm eff}$ variations simply with $\Delta \log T_{\rm eff}/\Delta \log L$ slopes. Therefore, in each TPC we fit $T_{\rm eff}$ as a function of L and the envelope mass $M_{\rm env}$, simultaneously, as $\log T_{\rm eff} = a_0 + a_1 \log L + a_2 M_{\rm env}$. The envelope mass $M_{\rm env}$ is computed through the current mass M and the core mass $M_{\rm core}$, as $M_{\rm env} = M - M_{\rm core}$. Besides the quantities at the quiescent stages, we also store the linear fitting parameters within each TPC of the original COLIBRI set of tracks, and interpolate them while going from the quiescent tracks to the isochrones. These interpolated fitting parameters allow us to easily convert the TPC L and $M_{\rm env}$ variations into $T_{\rm eff}$ variations.

$T_{\rm eff}$ variations computed in this way are illustrated in the middle panels of Figure 4. They clearly show the main change in the behavior of $T_{\rm eff}$ that occurs at the O- to C-rich transition. In the case of the younger isochrone (right panels), this event is further complicated by the strong mass loss that is associated with every one of its TP-AGB points.

Other stellar properties are interpolated and/or reconstructed along the TPCs in the isochrones, particularly the pulsation periods and chemical abundances. These are discussed later in Sections 3.4 to 3.5.

2.7. Further Computational Details

Although the scheme described and illustrated previously is quite general, a couple of additional details help us produce isochrone TP-AGB sections more closely resembling those of the original COLIBRI tracks. The first one is to adopt $\log M_{\rm i}$ as the independent variable in all interpolations involving mass, instead of $M_{\rm i}$; this choice produces smoother isochrones whenever the grids contain tracks widely spaced in $M_{\rm i}$, but in reality it makes little difference for the present, dense grids of tracks. The second detail is that, whenever two adjacent TP-AGB tracks contain a C-star phase, those tracks are split into two equivalent sections. In other words, we place an additional EEP at the O- to C-rich transition, hence imposing that the interpolations between tracks occur largely internally to their main O-rich and C-rich sections. In this way we avoid that the main change in $\Delta \log T_{\rm eff}/\Delta \log L$ slope between C- and O-rich stars causes artificial features in the shape of the derived isochrones.[9]

Moreover, we note that the TPC points are *not* inserted at evenly spaced intervals of $M_{\rm i}$ along the isochrones. Instead, they are more closely spaced at the beginning of the TPCs, which present the largest variations in $\log L$ (see Figure 4).

[9] Later on in the evolution, as the star loses most of its envelope and starts to heat in its way toward the planetary nebulae stage, the $\Delta \log T_{\rm eff}/\Delta \log L$ slopes change appreciably again, becoming even positive. This late change is also naturally present in the final section of the isochrones.

2.8. Spectral Libraries for Cool Giants

The PARSEC isochrones are transformed into absolute magnitudes via a series of bolometric correction (BC) tables, which are suitably interpolated in the $\log g$ versus $\log T_{\rm eff}$ plane, taking into account the surface chemical abundances, i.e.,

$$M_\lambda = M_{\rm bol} - {\rm BC}(X_i, \log g, \log T_{\rm eff}), \quad (2)$$

where $M_{\rm bol} = -2.5 \log(L/L_\odot) + 4.77$.

The formalism to derive the BC tables starting from libraries of synthetic spectra is fully described in Girardi et al. (2002, 2010).

For most stars, the X_i interpolation of Equation (2) means simply a linear interpolation in the variable [M/H]—hence a 3D linear interpolation in $\log T_{\rm eff} \times \log g \times$ [M/H] space. The main exception to this rule regards exactly the most luminous TP-AGB stars, which are treated according to a different scheme, reflecting the more extended sets of atmospheric models built to describe them.

2.8.1. Carbon-rich Giants

C-rich giants (with a surface carbon-to-oxygen ratio larger than 1, C/O > 1) have their atmospheres rich in carbon-bearing molecules like CN, C_2, C_3, HCN, and C_2H_2, presenting spectra significantly different than O-rich giants of similar parameters. For this reason, a separate database of C-rich spectra is needed. The Marigo et al. (2008) isochrones distributed since 2009 have used either the Loidl et al. (2001) or the Aringer et al. (2009) databases of synthetic C-rich spectra. For the present work, this library has been partially replaced: for solar metallicities (i.e., for the same content of heavy metals, excluding C and O) we implement a new set of spectral calculations provided by Aringer et al. (2016), based on the latest version of the COMARCS hydrostatic atmosphere models. This set comprises over 950 models with parameters in the ranges $4000 < T_{\rm eff}/{\rm K} < 2500$, $2 < \log g < -1$, C/O = [1.01, 1.05, 1.1, 1.4, 2.0], and masses of $M/M_\odot$ = [1, 1.5, 2, 3]. Most of the computed spectra, however, correspond to stars of low masses (1 and 2 $M_\odot$), with $\log g < 0$ and $T_{\rm eff} < 3400$ K, which are the intervals of parameters more relevant to describe the TP-AGB C stars observed in nearby galaxies.

The interpolation of BCs inside the C-rich grid follows the procedure outlined in Aringer et al. (2009): in short, the spectral properties are interpolated inside the multidimensional grid, with primary parameters being Z, $T_{\rm eff}$, $\log g$, and C/O. Then a small correction due to the spectral variations with mass is applied (which, for a fixed $T_{\rm eff}$ and $\log g$, corresponds to adopting an atmospheric model with a different sphericity).

In practice, the latest update in the C-star library affects all isochrones containing C-type stars at metallicities larger than [M/H] = −0.5. For these stars, the BCs will not only be based on the new models, but also benefit from the better interpolation inside a richer grid of models. In this context it should be noted that the new database also covers objects with C/O ratios as low as 1.01, while the smallest value in Aringer et al. (2009) was 1.05.

2.8.2. Oxygen-rich Giants

Regarding the "normal" O-rich stars (with C/O < 1), in previous releases the spectral database was either the ATLAS9-based from Castelli & Kurucz (2003) or the PHOENIX from

Allard et al. (2012; see Chen et al. 2014 for details), replaced by Fluks et al. (1994) for cool M giants. Aringer et al. (2016) has recently published a huge database of O-rich spectra derived from the COMARCS code, especially suited to describe the spectra of cool giants. Following the indications from this latter paper, we now adopt a smooth transition between the BCs derived from the previous databases, and those from Aringer et al. (2016), in the $T_{\rm eff}$ interval between 4000 and 5000 K ($4.6 < \log(T_{\rm eff}/{\rm K}) < 4.7$). This interval roughly corresponds to the CHeB phase (including the low-mass red clump) in solar-metallicity isochrones, and affects only the brightest RGB, TP-AGB, and RSG stars of metallicities [M/H] $\lesssim -1$. In most optical and infrared passbands, such a transition will appear completely smooth. Some artifacts might appear at UV wavelengths, where the different spectral libraries are provided with a very different sampling in λ. However, having precise UV photometry of cool stars is somewhat unlikely, so that this aspect might be less of a problem.

One of the most important consequences of adopting the Aringer et al. (2016) spectral library is that of having a more physically sound description of how the molecular lines vary as a function of stellar parameters. Especially important is the behavior of water lines, which heavily determine the near-infrared colors of O-rich giants; depending on their detailed behavior, near-infrared colors such as $J-H$ and $J-K_{\rm s}$ may not increase monotonically with decreasing $T_{\rm eff}$, as could be naïvely expected. This effect can be appreciated in Figure 5, which illustrates the changes we have in the 2MASS $J-K_{\rm s}$ colors of metal-rich O-rich giants, as a function of $\log T_{\rm eff}$ and $\log g$, for metallicities going from a third of solar to three times solar ([M/H] $= -0.5$, 0 and $+0.5$), and comparing present prescriptions based on Aringer et al. (2016) with those adopted in the previous Marigo et al. (2008) isochrones. As can be appreciated, $J-K_{\rm s}$ tends to reach an almost-constant value for the coolest giants, with $T_{\rm eff} \lesssim 3000$ K. The exact color of this "saturation," and the $T_{\rm eff}$ at which it occurs, depend heavily on the total metallicity—which is crucial in determining the efficiency of water formation—and mildly also on the chosen linelist (see Aringer et al. 2016 for details). Moreover, the $J-K_{\rm s}$ colors depend also on the exact $\log g$ reached by the giants; for the more compact giants (generally corresponding to the stars of lower initial mass stars found in older isochrones), there is even the possibility that the $J-K_{\rm s} \times T_{\rm eff}$ relation reverses, with the coolest giants becoming slightly bluer than the $T_{\rm eff} \sim 3000$ K ones. Figure 5 shows that this complex behavior is present in the new isochrones when the Aringer et al. (2016) spectral library is adopted.

All isochrones with O-rich sequences cool enough to enter in the $T_{\rm eff} \lesssim 3000$ K range will be affected by this change in the spectral library of O-rich giants. This especially applies to isochrones of solar and super-solar metallicity, like those illustrated in the middle and bottom panels of Figure 5. In isochrones of metallicities [M/H] $\lesssim -0.5$ dex (e.g., those in the upper panels of Figure 5), O-rich sections are generally hotter than this $T_{\rm eff}$ limit. Moreover, at smaller metallicities, a larger fraction of the TP-AGB appears as C-rich (see Section 3.6).

It is also interesting to note that the spectral library from Aringer et al. (2016), by including C/O ratios up to 0.97, approaches the region of parameters covered by S-type stars, in which the scarcity of free C and O and the enrichment of s-process elements provide a place for the appearance of molecular features of species such as ZrO and YO. More extended computations, fully covering the transition between C-, S-, and M-type spectra, will be provided in B. Aringer et al. (2016, in preparation).

One can also notice in Figure 5 that the present isochrones reach smaller $\log g$ and cooler $T_{\rm eff}$ than the $\log g < -1$, $T_{\rm eff} > 2600$ K limits of the Aringer et al. (2016) spectral library —especially at young ages (TP-AGB stars with HBB) or for very old and metal-rich isochrones. There is no easy solution for this problem, since the hydrostatic model atmospheres from COMARCS are both (a) hard to converge for stars of low $T_{\rm eff}$, and (b) not realistic, given the rise of high-amplitude pulsation and of huge convective cells at the stellar photosphere. Notice, however, that such very cool stars are rare, and that their observed properties are severely affected by circumstellar dust (see Section 2.9), hence little reflecting the detailed photospheric properties. However, for practical purposes these stars also need to be attributed a photospheric magnitude and color; we do so by simply extrapolating the BC tables linearly in the $\log g \times \log T_{\rm eff}$ plane.

2.9. Circumstellar Dust

On top of the photospheric spectra, our models include the effect of light reprocessing by circumstellar dust in the extended envelopes of mass-losing stars, for which we computed the radiative transfer (RT). The novelty in the present isochrones is the inclusion of a self-consistent treatment of dust growth, fully calculated as a function of the input stellar parameters (i.e., luminosity, actual mass, effective temperature, mass loss and elemental abundances in the atmosphere, as described in Nanni et al. 2013, 2014). Our dust growth description provides the dust mixture as a function of the stellar parameters as well as the optical depth at $\lambda = 1\mu$m. The dust code is coupled with an RT one (MoD by Groenewegen 2012a), based on DUSTY (Ivezic & Elitzur 1997). The most recent update of our dust growth model (Nanni et al. 2016) regards the production of carbon dust in circumstellar envelopes of C stars, which are particularly relevant for the interpretation of the colors of the so-called extreme AGB stars observed in infrared surveys of nearby galaxies (e.g., Boyer et al. 2011). Since in circumstellar envelopes of C stars the bulk of the dust produced is mainly composed by amorphous carbon, the dust temperature at the inner boundary of the dust zone is assumed to be the one of carbon dust, even if we also include silicon carbide (SiC) and iron dust in our calculations. For the same reason, for M stars the dust temperature at the inner boundary of the dust zone is assumed to be the one of the first silicate dust condensed (either pyroxene or olivine). For M stars the calculations also take into account the formation of Al_2O_3, quartz (SiO_2), periclase (MgO), and iron.

Therefore, the approach adopted allows us to compute BCs self-consistently as a function of stellar parameters, and provides the corresponding change in the broad-band absolute magnitudes and colors. A large grid of such models was computed, covering two values of masses (0.8 and 2 $M_\odot$); five of mass loss (from 10^{-7} to 10^{-5} $M_\odot\,{\rm yr}^{-1}$ at logarithmic spaced intervals); three luminosities ($\log(L/L_\odot) = 3.25$, 3.75, and 4.25); five $T_{\rm eff}$ (from 2600 to 3400 K); three metallicities ($Z = 0.001$, 0.004, and 0.008); and six values of carbon excess for C stars (with $8.0 < \log(n_{\rm C} - n_{\rm O}) - \log(n_{\rm H}) + 12 < 8.8$, where $n_{\rm C}$, $n_{\rm O}$, and $n_{\rm H}$ are the surface number fractions of carbon, oxygen, and hydrogen, respectively). The BC applied

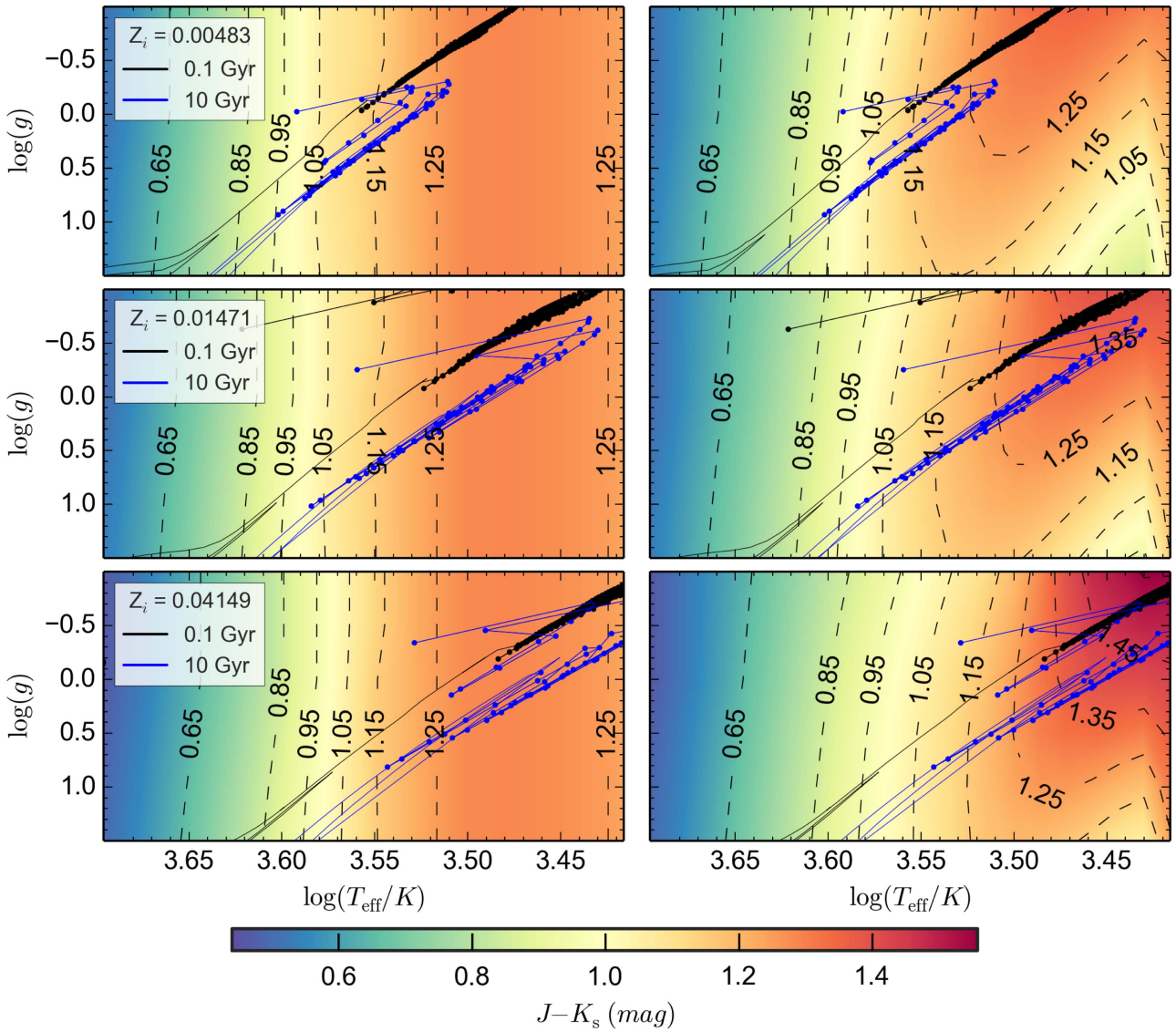

Figure 5. Map of the 2MASS $J - K_s$ colors attributed to O-rich giants of metallicities [M/H] $= -0.5$, 0, and $+0.5$ (top, middle, and bottom panels, respectively), as a function of $\log T_{\rm eff}$ and $\log g$ for two cases: the previous spectral library used in Marigo et al. (2008) (left panels), and the present one, which incorporates the Aringer et al. (2016) results (right panels). A couple of isochrones with ages of 0.1 and 10 Gyr and initial $Z_{\rm i} = 0.00483$ (top panels), $Z_{\rm i} = 0.01471$ (middle panels), and $Z_{\rm i} = 0.04149$ (bottom panels) are shown for comparison, displaying in particular the TP-AGB part—recognizable by the zig-zag during thermal pulse cycles, at $\log g \lesssim 0.5$. Only the O-rich section of these isochrones is plotted. We note in particular that with the present prescriptions (right panels), the colors of the coolest giants depend on $\log g$ and [M/H], while with the former prescriptions (left panels), only the dependence with $T_{\rm eff}$ was being considered.

to every star in the isochrones is determined via a multi-dimensional interpolation in this grid. For the O-rich stars, the models adopt the same parameters and optical data as in Nanni et al. (2013, 2014). For the C-rich stars, two grids are presently provided. One is computed using the Rouleau & Martin (1991) set of optical data with typical size of dust grains $\sim$0.1 μm, while the other is computed by employing Jager et al.'s (1998) data set produced at a temperature of 400 K with grains of size $\sim$0.06 μm. As detailed in Nanni et al. (2016), among several possible choices of optical data and parameters, these two are the ones that best reproduce the infrared colors of C stars in the SMC. However, larger deviations for the Rouleau & Martin (1991) optical data set are expected for the reddest colors, for which smaller grains ($\sim$0.06 μm) are better in reproducing the data.

The treatment of dust and RT adopted in this new release of isochrones represents a remarkable improvement with respect to the previous prescriptions assumed in Marigo et al. (2008), where the interpolation was performed for tables of spectra pre-computed for few dust mixtures (Bressan et al. 1998; Groenewegen 2006), since a full model for the growth and destruction of dust was still not developed.

2.10. Interstellar Dust

In addition, the effect of heterochromatic interstellar dust extinction is considered in the isochrones, as in Girardi et al. (2010). This means applying, to the points along the isochrones, the extinction coefficients which are a function not only of the passband being considered, but also of the stellar $T_{\rm eff}$; of the total extinction in the V band, A_V; and of the ratio between selective and absolute extinction R_V, as defined in Cardelli et al. (1989) and O'Donnell's (1994) generalized extinction curve.

Table 1
Coefficients for the Periods in Equation (3)

m	T	a	b	c	d
0	O	−0.683	1.874	−0.109	−1.957
0	C	−0.757	2.018	−0.121	−2.282
1	O	−0.585	1.620	0.083	−1.641
1	C	−0.499	1.515	0.107	−1.406

2.11. Long-period Variability

As demonstrated by extensive microlensing surveys of the Magellanic Clouds and Milky Way Bulge, TP-AGB stars are frequently observed as long-period variables (LPV), pulsating in at least one of several pulsation modes between the fourth overtone and the fundamental (Miras) mode (Lattanzio & Wood 2004; Wood 2015). LPV properties were introduced in isochrones for the first time in Marigo et al. (2008), using a series of fitting relations derived from Fox & Wood (1982), Wood et al. (1983), and Ostlie & Cox (1986) to describe periods in the fundamental and first-overtone modes (P_0 and P_1, respectively), as well as luminosity at which the dominant period changes between these modes. These relations are presently being revised with the aid of extensive calculations of pulsation models for a wide grid of input parameters, computed with the linear non-adiabatic radial oscillation code described in Wood and Olivier (2014). For the present work, we update the fitting formula for the predicted P_0 and P_1. They are of the form

$$\log(P_{\rm m}^{\rm T}/{\rm days}) = a\log(M/M_\odot) + b\log(R/R_\odot) + c\log(M_{\rm env}/M) + d, \quad (3)$$

where m stands for the mode (0/1 for fundamental/first overtone) and T for the chemical type (O- or C-rich). The fitting coefficients are presented in Table 1. These relations were derived from models along COLIBRI evolutionary tracks covering the $Z_{\rm i}$ interval from 0.002 to 0.017, and for masses between 0.8 to 2.6 $M_\odot$. The fitting relations provide periods accurate to within a few percent. Further updates and a thorough discussion will be presented in M. Trabucchi et al. (2016, in preparation). The likely transition luminosity between the first overtone to the fundamental mode was computed in the same way as in Marigo et al. (2008), based on Ostlie & Cox (1986).

Importantly, P_0 and P_1 pulsation periods are computed along the isochrones, but the periodic changes in the photometry are not taken into account. Therefore, the photometric properties we provide should be regarded as *mean properties* over the LPV pulsation periods, rather than instantaneous values.

3. RESULTS

Here we give just a quick overview of the main novelties in the present isochrones.

3.1. Surface Chemical Abundances along Isochrones

As noted previously, with this isochrone release we start providing detailed surface abundances $\{X_i\}$—presently consisting of the mass fractions X, Y, Z, $X_{\rm C}$, $X_{\rm N}$, and $X_{\rm O}$—along the isochrones. These values are all interpolated linearly (always using the EEPs as a reference) from those given along the evolutionary tracks. Their values change as a result of microscopic diffusion (especially during the main sequence of low-mass stars), of dredge-up events, and of HBB at the most massive TP-AGB stars. Figure 6 illustrates the regions of the HR diagram that are most affected by these changes, for a set of given initial metallicity, by showing the changes in the total metal content by mass, Z. The main changes in Z occur at the main sequence of low-mass stars due to microscopic diffusion (the purple area), and at the TP-AGB due to third dredge-up events (the yellow-to-red sections at the top). In addition, the isochrones also contain the variations in Z due to the second dredge-up in intermediate-mass stars, and the almost-imperceptible variations along the RGB due to protons locked up in CNO nuclei, which appear after the first dredge-up.

Figure 7 illustrates one of the many possible applications of the new abundance information: its left panel presents the expected correlation between the number ratio of C and N as compared to the Sun, [C/N], and the age of RGB stars. This relation results from the first dredge-up in low-mass stars, as discussed in Salaris et al. (2015). As can be seen, it presents a clear dependence on the initial metallicity, which is also well understood.[10] Such a relation is nowadays, directly or indirectly, being used to constrain ages of field MW stars (see Masseron & Gilmore 2015; Martig et al. 2016; Ness et al. 2016). Having C and N abundances tabulated in grids of isochrones means that the observed samples of field RGB stars can be more easily modeled via population synthesis approaches, giving us the possibility to check for possible biases or contaminants in the observations.

Despite the potential importance of the [C/N] versus age relation, its empirical verification has been somewhat limited thus far. Salaris et al. (2015) present a comparison between the [C/N] results from BaSTI models and data for five open clusters, plus a point representative of the halo field; although the general trend with age is confirmed, the comparison clearly suffers from the few observational points, from the large abundance errors, and likely from the heterogeneity of the cluster data.

3.2. Surface Chemical Abundances along TPCs

Another main novelty in the present isochrones is the presence of detailed information regarding the stellar changes —in L, $T_{\rm eff}$, and $\{X_i\}$—along TPCs. We note that Marigo et al. (2008) isochrones with TPC variations have already been distributed upon request in the past, but are now provided as a ready-to-use option in the new web interface.

Figure 4 shows how the TPCs appear in the $M_{\rm i}$ versus $\log L/L_\odot$ diagram of two isochrones, illustrating (1) the notable differences in the shape of TPCs between low- and intermediate-mass stars (see also Boothroyd & Sackmann 1988; Vassiliadis & Wood 1993), and (2) the sizeable variations in surface chemical compositions along these isochrone sections.

This aspect of providing chemical abundance changes along TPCs deserves a more detailed description. Let us start with the simplest case: low-mass stars in which only 3DU is operating. In the original evolutionary tracks, the surface chemical composition of these stars changes soon after the He-flash that initiates the TPC (i.e., at a phase $\phi = 0$), and stays constant

[10] The somewhat different slope for the youngest isochrones of [M/H] = 0.5 dex likely results from its very high initial helium content, $Y_{\rm i} = 0.32$.

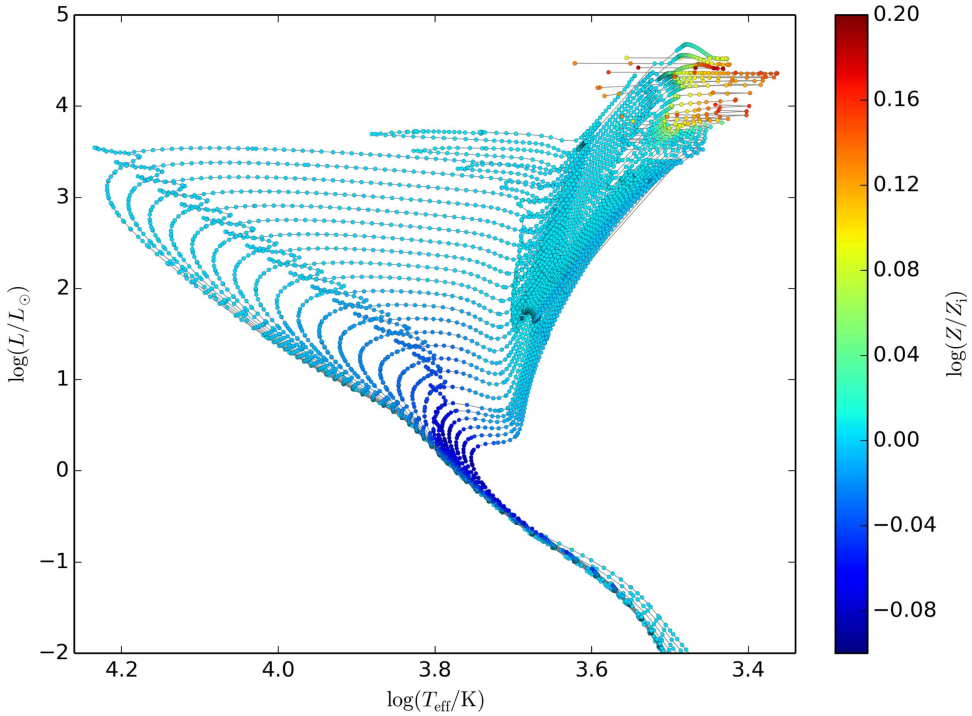

Figure 6. Changes in the current surface metal content Z across the HR diagram, for a set of isochrones of initial $Z_{\rm i} = 0.01471$, with ages varying from $\log(t/{\rm yr}) = 7.8$ to 10.1 at steps of 0.1 dex, and for $n_{\rm inTPC} = 0$.

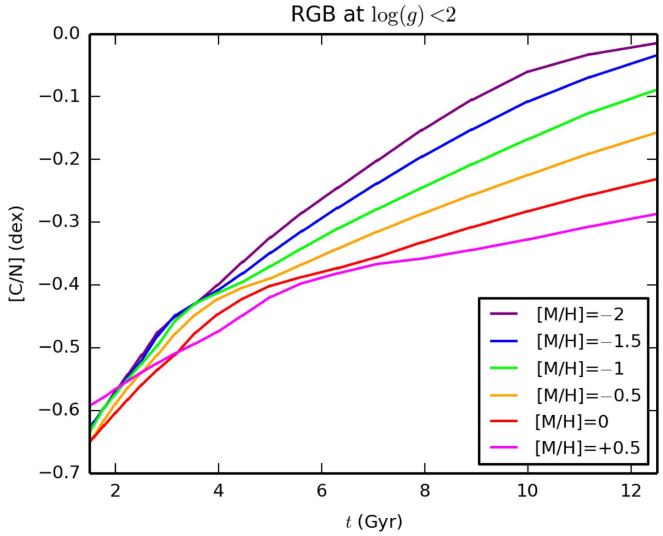

Figure 7. The predicted variation of [C/N] with age in RGB stars of a few selected metallicities.

along the entire TPC until its end, just prior to the next He-flash (at $\phi = 1$). In the isochrones, our interpolation algorithm transforms this step-by-step change in the surface abundances into a gradual change, as can be appreciated in the left panels of Figure 4. This feature is intentional: indeed, our isochrones aim at explaining the expected surface abundances in large populations of TP-AGB stars, in a statistical way, and not the behavior that happens in every individual TP-AGB star as it evolves. In fact, the important point in this case is that the general trend of varying abundances with the main stellar parameters—mass, age, luminosity, and so on—is preserved by our interpolations.

In the case of the more massive intermediate-mass stars, in addition to 3DU, HBB changes the abundances (and sometimes also the spectral type) along every single TPC. This feature also needs to be reproduced in the isochrones, since it causes a correlation between the chemical composition and other stellar properties; for instance, it causes stars found in their low-luminosity dip phases of a TPC to be more likely C stars than stars found in brighter, quiescent phases, even if other stellar properties (age, core mass, initial mass and metallicity, and so on) are similar. Therefore, we also include this effect in the isochrones, by distributing the in-cycle abundance changes caused by HBB, $\Delta(X_i)$ (in which values are also interpolated among TP-AGB tracks of all masses and metallicities), along every single TPC re-created in the isochrones. The result can be appreciated in the right panels of Figure 4, which show an isochrone section where C/O transits several times between values lower and higher than 1.

3.3. $n_{\rm inTPC}$ and the General Appearance in Color–Magnitude Diagrams

Figure 8 illustrates a set of isochrones of initial metallicity [M/H] $= -0.4$ dex ($Z_{\rm i} = 0.006$) and covering a wide range of ages, in the HR diagram. The different panels show how the TP-AGB sections of the isochrones appear for different values of $n_{\rm inTPC}$. The initial case of $n_{\rm inTPC} = 0$ corresponds to smooth isochrones, containing only the quiescent points of TPCs—similarly to those distributed by Marigo et al. (2008). The isochrones with $n_{\rm inTPC} = 5$ already contain a fair amount of detail about TPCs, including its most important feature: the relatively long-lived low-luminosity dips, which are described by a set of three points in every TPC. In isochrones with $n_{\rm inTPC} = 25$ the L–$T_{\rm eff}$ variations are described in greater detail; their low-luminosity dips appear as smooth sequences, and they present slightly more detailed high-luminosity peaks. Therefore

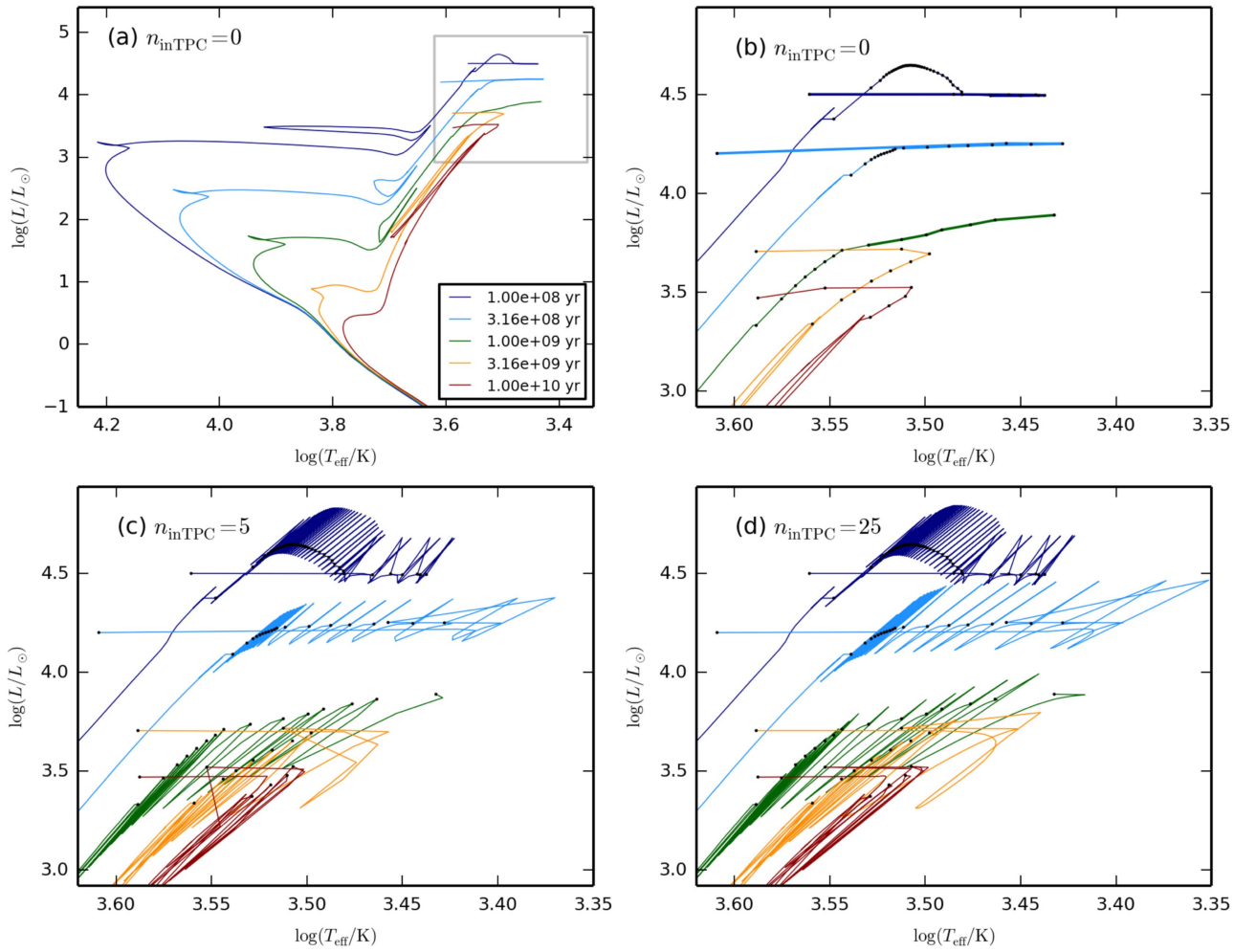

Figure 8. Examples of isochrones in the HR diagram, for a fixed metallicity ([M/H] = −0.4 dex, or $Z_{\rm i} = 0.006$) and five different ages at equally spaced $\Delta \log t = 0.5$ dex intervals. Panel (a) shows a large section of the HRD for isochrones computed with $n_{\rm inTPC} = 0$—that is, without the details of TPCs. Panels (b) to (d) zoom in on the TP-AGB region of panel (a), showing a sequence of increasing $n_{\rm inTPC}$. The small black dots mark the position of quiescent points along the TPCs. On panel (b) only, the C-rich section of the isochrones is drawn with a heavier line.

one can set the following general guidelines regarding the $n_{\rm inTPC}$ value: in simple applications that just require an overall description of the main loci of TP-AGB stars (for instance, looking at variations in the C-rich sequences with age, as in panel b of Figure 8), one can use $n_{\rm inTPC} = 0$. But for a fair description of the main strips occupied by TP-AGB stars in different diagrams, one needs to consider the well-populated low-luminosity dips, for which a $n_{\rm inTPC}$ of at least 5 is recommended. For more detailed population studies aimed at accurately reproducing star counts, $n_{\rm inTPC}$ can be increased to values as high as >20.

This point is illustrated further in Figure 9, which presents the same isochrones in the popular $K_{\rm s}$ versus $J - K_{\rm s}$ diagram of 2MASS photometry. The isochrones with $n_{\rm inTPC} > 0$ present CMD sequences significantly broadened due to the TPCs, as expected. Remarkably, along the extreme AGB region, the $J - K_{\rm s}$ color variations inside TPCs become so wide that increasing $n_{\rm inTPC}$ to 25 does not suffice to transform the isochrone features into smooth lines. Therefore, the most suitable value of $n_{\rm inTPC}$ may also depend on other additional factors like the wavelength of the observations to be interpreted, their photometric depth and typical photometric errors, and so on. For all these reasons, $n_{\rm inTPC}$ is kept as a free parameter in our codes and web interfaces.

That said, it is interesting to note how O- and C-rich stars are predicted to distribute in different regions of the HRDs and CMDs in Figures 8 and 9. First of all, there is the well-known fact that a C-rich phase is only found in isochrones younger than a few Gyr. In addition, in the HRD, there is an evident trend of C stars being found at smaller $T_{\rm eff}$ than O-rich stars; this effect is caused by the sudden increase in Rosseland mean opacities as C/O overcomes the value of 1 in stellar atmospheres (Marigo 2002; Marigo et al. 2013). In the $JK_{\rm s}$ CMD, the bulk of C stars separates even more from the O-rich ones: most O-rich stars tend to distribute along a broad diagonal sequence that extends from $[K_{\rm s}, J - K_{\rm s}] = [-6, 1.0]$ to $[-10, 1.4]$. C stars instead clearly draw a separate sequence departing from the O-rich one at $[-7, 1.3]$ and reaching $[1.8, -9]$. The latter is caused, in addition to the $T_{\rm eff}$ changes, by the different spectral features of C and M stars, including those caused by circumstellar dust.

All these features became well-known since the release of near-infrared photometry for the Magellanic Clouds (e.g., Cioni et al. 2000; Nikolaev & Weinberg 2000). A very preliminary comparison with 2MASS data for the inner LMC is presented in Figure 9, just evincing a few facts: for example, the TP-AGB sections of the younger isochrones (with ages 1 to 3.16×10^8 years) have very few counterparts in 2MASS data;

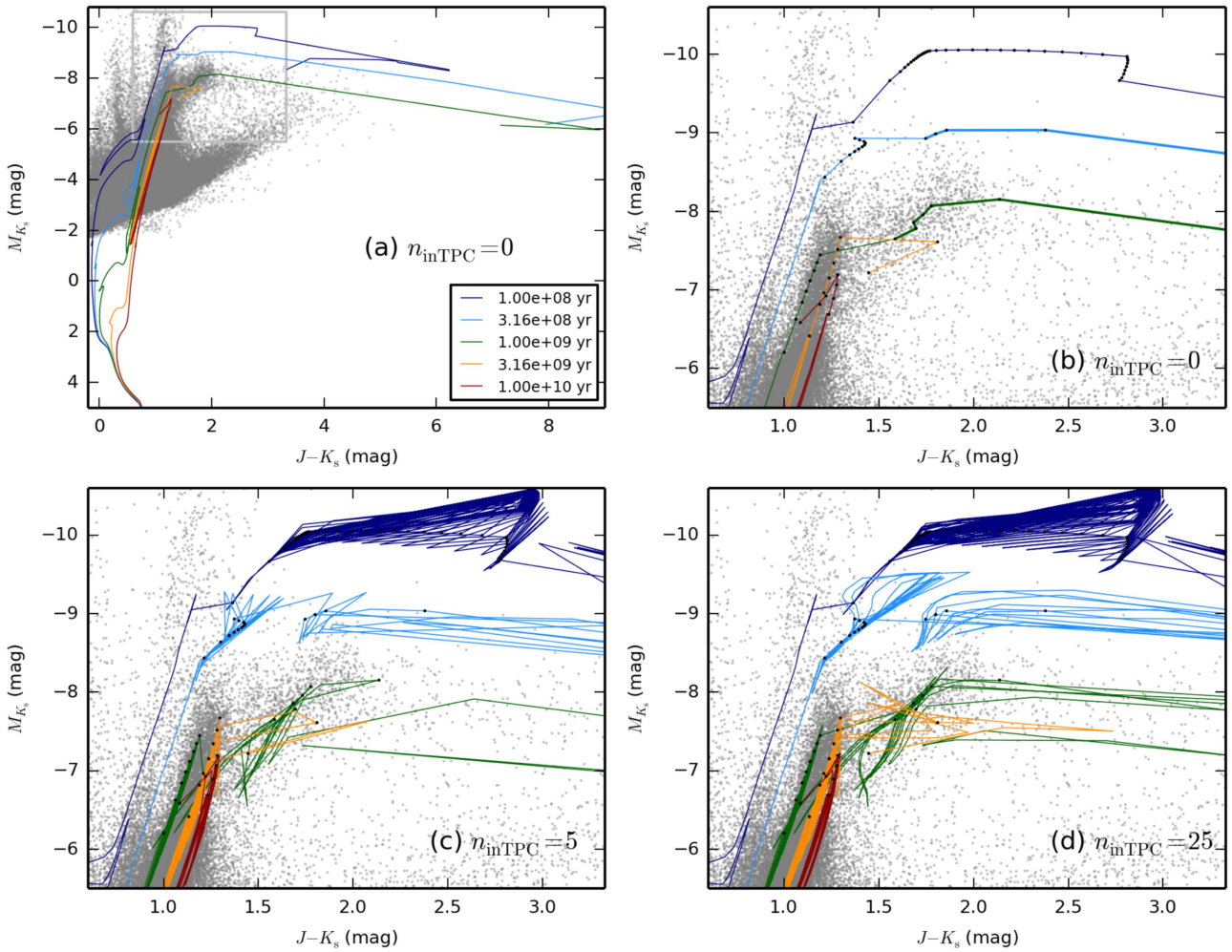

Figure 9. The same as in Figure 8, but for the classical CMD of 2MASS photometry, M_{K_s} vs. $J-K_s$. Gray points in the background are the 2MASS point sources (Skrutskie et al. 2006) within 1° of the LMC center, as determined by van der Marel & Cioni (2001); they are shifted by a true distance modulus of 18.5 mag, whereas extinction is ignored.

this is likely caused by the fact that these TP-AGB sections, being derived from TP-AGB models with small lifetimes, actually span very narrow intervals in initial mass. Isochrones with ages larger than 1 Gyr instead have clear correspondence in the overall distribution of observed points. The most prominent features in these diagrams, in addition to the tip of the RGB (TRGB) at −6.5, are

1. The well-populated and diagonal sequence of O-rich AGB stars extending from the TRGB up to $M_{K\rm s}$ and at $J-K_{\rm s}<1.3$, which is well matched by the isochrones with $t>1$ Gyr.
2. An upward, less-populated extension of this O-rich sequence up to −9.5, with an upper part well matched by our 3.16×10^8 years isochrone.
3. The red tail of C-rich stars extending up to $J-K_{\rm s}\sim2$, which is well described by the C-rich section of our 1-Gyr isochrone.
4. The scarcely populated and extended "extreme AGB" region, defined by $J-K_{\rm s}>2$, with a slope that is well matched by our isochrones with ages 3.16×10^8 and 10^9 years.

This qualitative comparison with 2MASS does not consider the expected occupation probability of every isochrone section—which can be easily derived from the isochrone tables—as well as other fundamental aspects such as the initial mass function (IMF) and history of star formation and chemical enrichment in the LMC. A detailed quantitative comparison with the Magellanic Clouds' data will follow in separate papers.

As a cautionary note, we highlight that the appearance of the extreme AGB sequences in the CMD is still affected by limitations in our present grids of RT models: since they do not cover the entire range of parameters found in the tracks, models with the most extreme L, C/O, $\dot{M}$, and $T_{\rm eff}$ have their properties badly determined. This applies especially to the stars at the top-right boundary of the "extreme AGB" region, corresponding just to the youngest isochrones in Figure 8, with an age of 10^8 years. This problem, other than temporary (since RT models are being expanded) is not a major one if we consider that just a minority of the AGB stars observed in nearby galaxies are expected to be affected.

3.4. Period Changes along TPCs

In the isochrone TP-AGB sections, pulsation periods change from point to point according to Equation (3), thanks to the large changes in M, L, $T_{\rm eff}$, and $\{X_i\}$, both between isochrones and inside TPCs of single isochrones. Although the pattern of these changes can be rather complicated, a few general trends can be drawn here, with the help of Figure 4. At low

luminosities and relatively high $T_{\rm eff}$, the dominant pulsation mode is the first-overtone one, of a shorter period. Most isochrone TP-AGB sections will start with this dominant mode. Later along the isochrone, a transition to a dominant fundamental mode (longer period) can occur. As illustrated in the bottom panels of Figure 4, the transition happens along a few TPCs. In the isochrones of intermediate-age populations, the transition from the first-overtone to fundamental mode often coincides with the main transition from O- to C-rich phases, where a marked reduction of the $T_{\rm eff}$ takes place (Marigo 2002; Marigo & Girardi 2007); whenever this happens, however, there are always small C-rich sections expected to appear in the first-overtone, as there are O-rich sections expected in the fundamental mode.

For younger isochrones where the TP-AGB develops at high luminosities and cool $T_{\rm eff}$s, larger sections of the isochrones appear with a dominant fundamental mode. This includes most of the stars undergoing HBB, with their characteristic high L and low C/O ratio.

In reality, the situation is more complex, with stars appearing in multiple pulsation modes and in higher-order overtones. More complete modeling of these sequences is underway (M. Trabucchi et al. 2016, in preparation), and will be taken into account in subsequent releases of the isochrones. For the moment, it suffices to mention that our predictions for the fundamental mode pulsation seem more robust, since in this case both the entrance (via the transition luminosity given by the Ostlie & Cox 1986 relation) and the final exit (usually via mass loss) from the FM sequence are modeled consistently. The same cannot be said of the first overtone, for which there is not yet a physically based prescription defining the moment stars enter on this pulsation mode.

3.5. Other Quantities Added In (or Cleared From) the Isochrone Tables

The present isochrone tables present a few other useful quantities derived from the previously mentioned ones—for instance, the surface gravity g and the radius R, which are simply derived by means of its physical definition and from the Stefan-Boltzmann law, respectively. There is also a label to identify the main evolutionary stages (pre-main sequence, main sequence, subgiant branch, RGB, CHeB, early-AGB, TP-AGB), as well as the last point on the TP-AGB. Also given are TP-AGB specific quantities like the C/O ratio (in number), the C excess in C-rich stars (see Eriksson et al. 2014, for its precise definition), the mass loss rate, the optical depth of the circumstellar dust at 1 μm, the LPV periods, and pulsation modes.

With respect to Marigo et al. (2008), we have also been more careful about the range of applicability of some tabulated stellar properties, and about their names. In particular,

1. Pulsation periods and modes of long-period variables are presented just for TP-AGB stars; otherwise they are set to null and -1, respectively. Indeed, while the relations used to compute periods and modes may also apply to bright RGB and RSG stars, they have not been tested for those stars. Moreover, they would not provide reliable periods for fainter variables like classical Cepheids and RR Lyrae.
2. Presently, we keep track of the H-exhausted core masses only along the TP-AGB phase, where this quantity is useful for determining the properties of TPCs. Therefore, core masses are named as $M_{\rm core,TP}$. They are set to null for any evolutionary phase previous to the TP-AGB.
3. Likewise, the dust optical depth, $\tau(1\ \mu{\rm m})$, is set to null for all evolutionary phases previous to the TP-AGB, even if their mass losses are significant (as close to the tip of the RGB phase). The reason for this choice is that the mechanism for dust formation may act differently in other stars, and may even be inefficient in RGB stars (Gail & Sedlmayr 1998). Moreover, present-day claims of detection of circumstellar dust shells around RGB stars, as well as their interpretations in terms of mass loss, are still either controversial (see Boyer et al. 2010; Momany et al. 2012, and references therein) or dependent on observations of very small samples of nearby stars (Groenewegen 2012b).

All these points may be revised in future releases of these isochrones, as the theoretical prescriptions are replaced and/or expanded, and other useful quantities and abundance information are added to the tables.

3.6. TP-AGB Bulk Properties

A notable difference of the new TP-AGB tracks computed with the COLIBRI code, compared to those of Marigo & Girardi (2007), is related to the duration of the TP-AGB phase. These differences are illustrated in detail in the recent review by Marigo (2015) and in Rosenfield et al. (2016). A particular prediction is that the number of C stars make an "island" in the metallicity versus age plane—that is, their formation is strongly favored at ages peaking at $\sim$2 Gyr and at metallicities $-1 < [{\rm M/H}] < 0$, while they nearly disappear at all other extremes of the age–metallicity plane. This prediction is well described in Figure 7 of Marigo (2015), which shows a map of the TP-AGB lifetime of the C stars expected at every age and metallicity.

With the detailed isochrones, we can check these predictions in more detail. First of all, we can eliminate the approximation (widely adopted since Frogel et al. 1990, and implicitly assumed in Marigo 2015) that the number of TP-AGB stars in a stellar population is proportional to the lifetime of the TP-AGB tracks with the same turn-off mass. Indeed, Girardi et al. (2013) demonstrated that this approximation badly fails at ages close to 1.6 Gyr when a rapid change in core He-burning lifetimes causes a marked spike in the production rate of TP-AGB stars (the "AGB-boosting" effect; see also Girardi & Bertelli 1998). Moreover, another difference with respect to previous works regards the youngest isochrones containing TP-AGB stars with HBB, for which we can now separate C- and M-type stars along individual TPCs (Figure 4), and correctly compute their mean properties.

Thus, Figure 10 shows the expected number of different kinds of TP-AGB stars per unit mass of stars formed in a stellar population, as a function of age and metallicity. These quantities derive from the simple integral

$$N^{j}_{\rm TPAGB}(t,\,Z) = \int_{(t,Z)}^{j} \phi(M_{\rm i})\,dM_{\rm i}, \qquad (4)$$

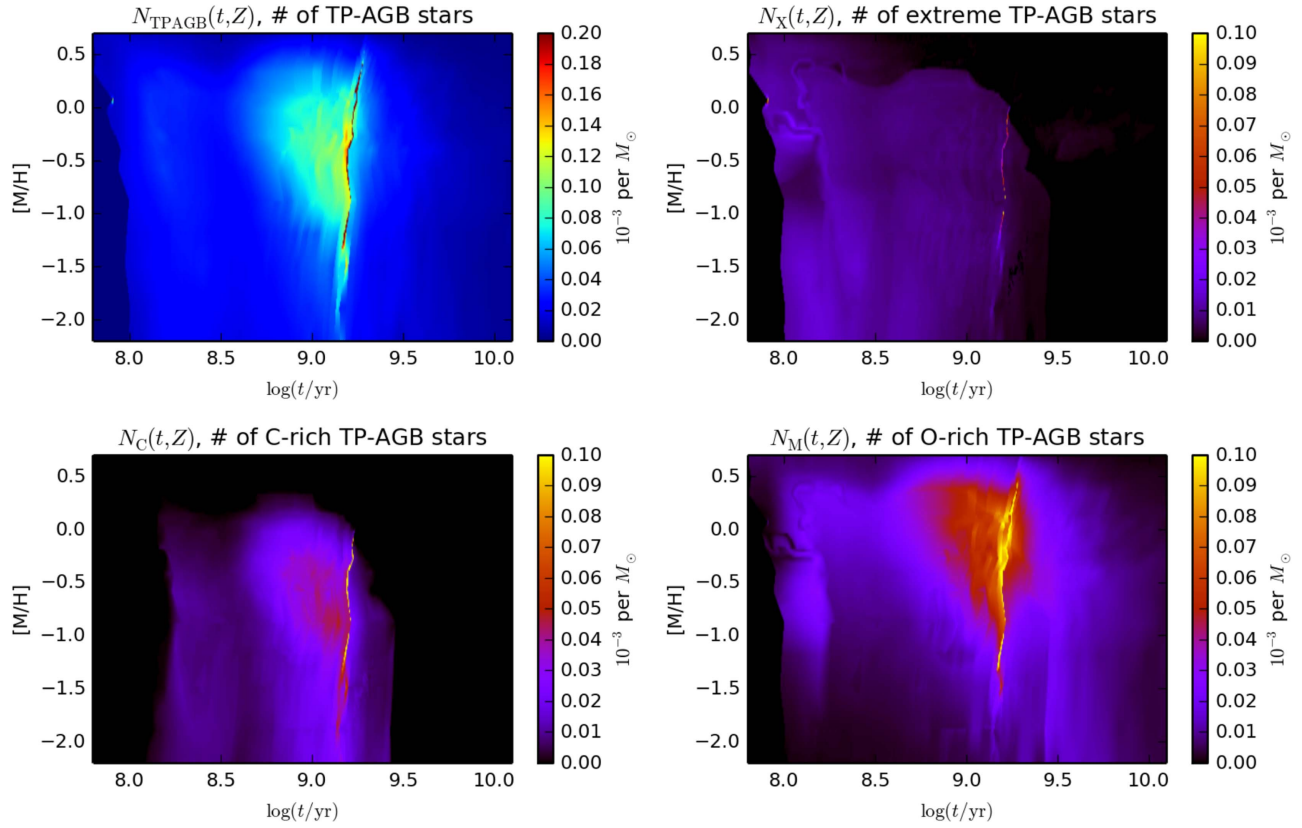

Figure 10. Map of the the expected numbers of TP-AGB stars as a function of the initial metallicity and age, per unit mass of formed stars in a stellar population. They have been computed using the Kroupa (2002) IMF, and adopting very simple criteria for the identification of C, M, and extreme TP-AGB stars. The first panel also presents, on a distinct color scale, the total numbers of TP-AGB stars. See the text for more explanation.

where $\phi(M_{\rm i})$ is the IMF by number, normalized to a unit total mass, i.e.,

$$\int_0^\infty M_{\rm i}\,\phi(M_{\rm i})\,dM_{\rm i} = 1\,M_\odot, \tag{5}$$

and the integral is performed over the isochrone sections j that satisfy the desired criterion. In practice, this calculation is greatly facilitated by the isochrone tables being produced as sequences of increasing initial mass $M_{\rm i}$, and including tags for the evolutionary stage that clearly indicate isochrone sections where the TP-AGB phase is either starting or terminating. This allows us to easily replace the integral by a summation that only considers the pairs of subsequent points that satisfy the condition j.

For the sake of illustration, we consider four simple criteria in Figure 10. The first one illustrates the total numbers of TP-AGB stars ($N_{\rm TP}$). Then three criteria were designed to separate these TP-AGB in broad categories: those of extreme TP-AGB stars ($N_{\rm X}$, with $J-K_{\rm s}>2$ mag), which generally have mass loss rates in excess of $|\dot{M}|>10^{-6}\,M_\odot\,{\rm yr}^{-1}$ and are optically obscured by their circumstellar dust shells, plus those of optically visible C and M-type TP-AGB stars ($N_{\rm C}$ and $N_{\rm M}$, with $J-K_{\rm s}<2$ mag and C/O >1 and C/O <1, respectively). Of course, these definitions do not correspond precisely to those adopted in analyses of observed samples; however, similar estimates can be easily derived from the available isochrones, using alternative criteria based on the photometric or chemical properties of stars.

There are some remarkable aspects in the maps presented in Figure 10:

1. First, it is evident that optically visible C stars appear over a limited area of the metallicity–age plane, being absent at all ages $t>4$ Gyr. This limit is essentially caused by the low efficiency (or absence) of third dredge-up in stars of low masses. It also corresponds to a classical observational fact—namely the absence/scarcity of bright C stars (i.e., with luminosities clearly above the tip of the RGB) in the oldest clusters of the Magellanic Clouds, which has become clear since the compilation by Frogel et al. (1990). Indeed, the oldest LMC cluster to clearly contain such C stars is NGC 1978, with six likely members and an age of about 2 Gyr (Mucciarelli et al. 2007). In the SMC, the oldest case is Kron 3, with three likely members and an age of ≈6.5 Gyr (Glatt et al. 2008a).[11]
2. C stars are also absent in young metal-rich populations, and become progressively more frequent in young populations of metallicity [M/H] <-0.5 dex. This absence at young ages is caused mainly by HBB in the more massive TP-AGB stars, preventing a transition to the C-rich stage while the star is still optically visible. This is also observed in the form of a paucity of C stars in young Magellanic Cloud clusters, as first noticed by

[11] The SMC clusters NGC 339 and NGC 121, with ages of about 6.5 and 11.5 Gyr, respectively (see Glatt et al. 2008a, 2008b), have 1 C star each. However, these are underluminous objects and might correspond to the result of binary evolution, which is not being considered here.

Frogel et al. (1990). Although the data are severely affected by the low number statistics and the uncertainties in the field contamination,[12] they is compatible with no visible C stars being observed in clusters younger than about 300 Myr (turn-off masses larger than $3\,M_{\odot}$; see Figure 1 in Girardi & Marigo 2007).

3. Finally, C stars are absent from very metal-rich populations, with metallicities $[\mathrm{M/H}] > 0.4$ dex. This is caused both by more carbon dredge-up being needed to cause the transition to $\mathrm{C/O} > 1$, and by the third dredge-up being weaker at higher metallicities. Conclusive evidence for this metallicity ceiling for the C-star formation has been recently found by Boyer et al. (2013) using *Hubble Space Telescope* medium-band observations of the inner M 31 disk. More specifically, they found that a population with mixed ages and a mean metallicity of $[\mathrm{M/H}] \approx 0.1 \pm 0.1$ dex has an extremely low number ratio between C and M stars, $\mathrm{C/M} = (3.3^{+20}_{-0.1}) \times 10^{-4}$.
4. A very unusual feature in all these $N^j(t, Z)$ plots is the nearly vertical "scar" or "lightning" at ages close to $\log(t/\mathrm{yr}) \simeq 9.2$, which corresponds to the AGB-boosting effect described by Girardi et al. (2013). The effect is determined by the rate at which stars leave evolutionary stages *previous* to the TP-AGB; hence it appears indistinctly for all TP-AGB subsamples—and nearly at the same age interval. It should be noticed, however, that the effect is extremely brief. It appears clearly in these plots thanks to their very fine age resolution (namely, $\Delta \log t = 0.005$ dex). Girardi et al. (2013) claims that this effect contributes to the maximum relative numbers of AGB stars observed in stars clusters, such as NGC 419, NGC 1806, NGC 1846, NGC 1751, and NGC 1783, all with mean turn-off ages around 1.7 Gyr.
5. With the exception of the AGB-boosting period, the TP-AGB production broadly peaks at ages between 1 and 2 Gyr. This feature is determined by the maximum TP-AGB lifetimes being reached for stars of initial masses in the range 1.5 to $2\,M_{\odot}$ (Marigo et al. 2003; Marigo & Girardi 2007). This feature also agrees with the maximum numbers of these stars, relative to the integrated cluster luminosity, being found in clusters with turn-off masses broadly located between 1.6 and $3\,M_{\odot}$ in the LMC (Girardi & Marigo 2007).
6. Extreme AGB stars are more frequent at the youngest ages, where TP-AGB stars reach higher luminosities and have larger envelopes to lose through mass loss. They become much rarer at ages exceeding 2 Gyr. It is hard to check this prediction quantitatively, since just a handful of Magellanic Cloud clusters contain extreme AGB stars, and usually just a few units per cluster (Tanabé et al. 2004; van Loon et al. 2005). It is remarkable, however, that among the 30 stars with IR-excess likely belonging to clusters identified by van Loon et al. (2005), none is found in objects older than 3 Gyr (with turn-off masses smaller than $1.3\,M_{\odot}$), even if such clusters comprise ∼10% of the total mass of their sample (see their Table 9).

Given the uncertainties both in the models and in the data—the latter mostly regarding the field contamination, but also including uncertain age and metallicity estimates—any comparison between them should be regarded just as a preliminary check of the mean trends.

3.7. The AGB-boosting Period

Regarding item 4 listed previously, we are completely aware that the AGB-boosting effect is in general absent from other published sets of isochrones in the literature. As discussed in Girardi et al. (2013), the effect appears only if a fine mass resolution is adopted for the computation of the grids of evolutionary tracks, and if the interpolation between the tracks is properly dealt with, as a result of a quick decrease of CHeB lifetimes at ages of ∼1.6 Gyr. It is interesting to note that these conditions have been recently confirmed by Choi et al. (2016), with an independent set of evolutionary tracks. For works of evolutionary population synthesis of galaxies, this feature can be seen as an unnecessary complication, and it can be even intentionally suppressed (see, e.g., Dotter 2016). However, as demonstrated in Girardi et al. (2013), this period of intense TP-AGB production is an unavoidable consequence of the rearrangements in stellar lifetimes that appear as electron degeneracy develops in the H-exhausted cores of low-mass stars; it really corresponds to light emitted by stars that has to be taken into account into the evolution of the bulk properties of stellar populations. Moreover, this feature is probably very important for the interpretation of the most classical TP-AGB calibrators, namely the intermediate-age star clusters in the Magellanic Clouds (Girardi et al. 2013), which in turn affect the calibration of the role of TP-AGB stars in population synthesis models themselves.

That said, it is a matter of fact that the AGB boosting is a quick event in the life of stellar populations, lasting for no longer that a few 10^8 years, so that it may appear or not, depending on the exact values of ages chosen for producing isochrones around the 1.6 Gyr age interval. This point has been extensively discussed and is well illustrated in Figure 4 of Girardi et al. (2013). Therefore, a careful selection of the age values and age bins might be necessary in order to have a fair account of the TP-AGB star counts and of their integrated light in population synthesis models of galaxies.

As discussed in Girardi et al. (2013), based on isochrones derived from PARSEC tracks computed with a mass spacing of $\Delta M_{\mathrm{i}} = 0.01\,M_{\odot}$, the AGB-boosting period turns out to last for $\Delta t_{\mathrm{boost}} \approx 10^8$ years (see their Figure 4), yielding numbers of TP-AGB stars, $N^j(t)$, a factor $A_{\mathrm{boost}} \approx 2$ larger than at immediately younger and older ages. The presently released isochrones, instead, are derived from tracks computed with $\Delta M_{\mathrm{i}} = 0.05\ M_{\odot}$ in the mass range of interest here (at the boundary between RGB+HB and INT tracks in Figure 1, or $M_{\mathrm{i}} \sim 1.75\ M_{\odot}$). This situation tends to produce AGB-boosting periods that are very short-lived (i.e., $\Delta t_{\mathrm{boost}}$ is just a fraction of $\approx 10^8$ years) but produce a more pronounced spike in the TP-AGB numbers (hence a larger A_{boost} factor). The product of $\Delta t_{\mathrm{boost}} \times A_{\mathrm{boost}}$, however, seems to be roughly conserved, irrespective of the mass resolution of the tracks—provided that this resolution is good enough to include the rise in the He-burning lifetimes that occurs at $M_{\mathrm{i}} \simeq 1.75\ M_{\odot}$. We have verified that, given the present tracks with $\Delta M_{\mathrm{i}} = 0.05\,M_{\odot}$,[13] the coarsest age resolution necessary to detect the spike in

[12] The most impressive exception is the single C star observed in the core of the ≈50-Myr-old cluster NGC 1850, which in the absence of independent indications for its membership, has usually been ascribed to the underlying LMC field.

[13] It is our intention to further improve this mass resolution in future releases of the PARSEC–COLIBRI isochrones.

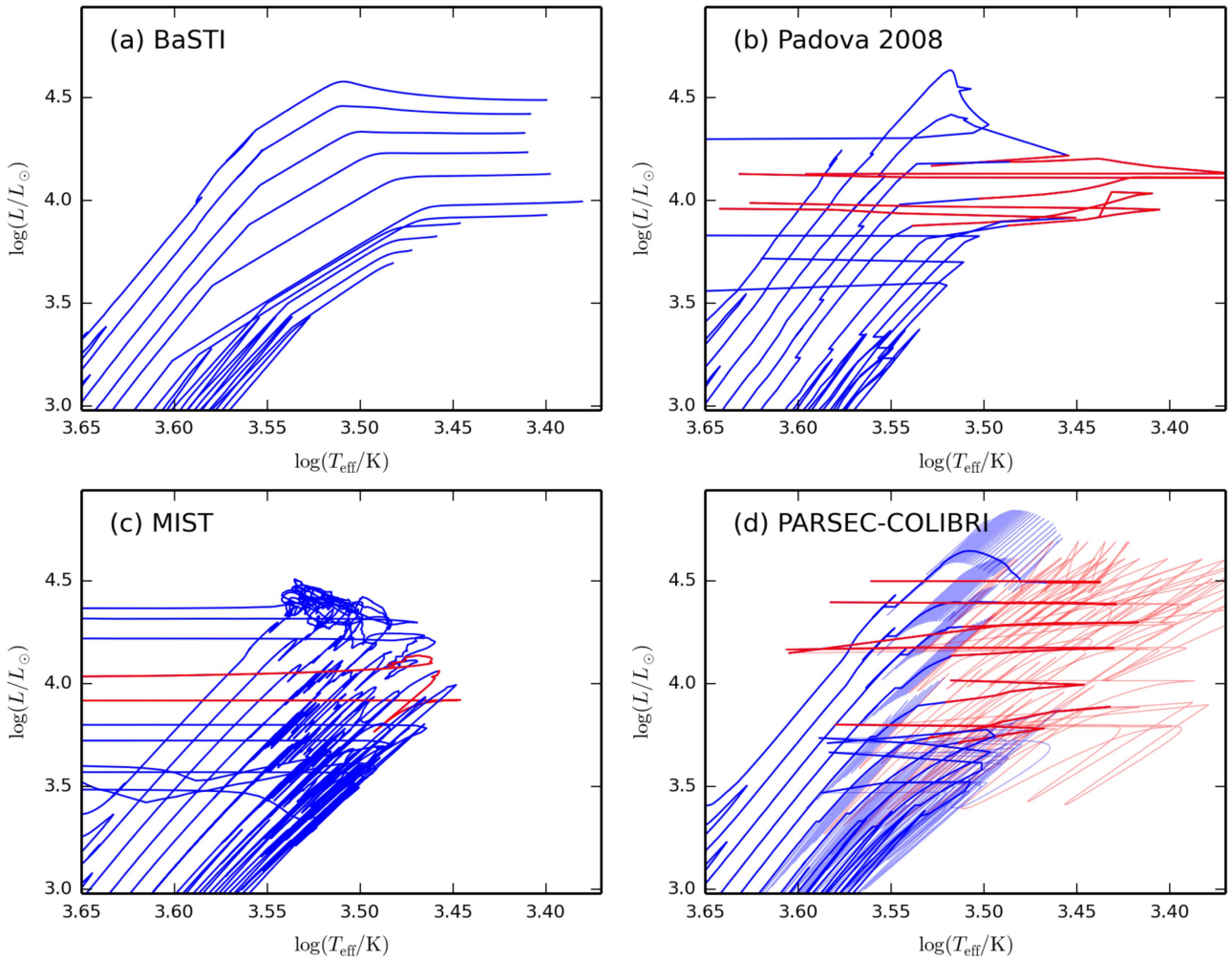

Figure 11. Comparison between available isochrones, including the complete TP-AGB phase, in the HRD. All sets include convective core overshooting, and have a metallicity close to that of young LMC populations. In each panel, ages go from $\log(t/\mathrm{yr}) = 8$ to 10 at intervals of 0.2 dex, from top to bottom. O-rich sequences are marked in blue; C-rich ones are marked in red. (a): BaSTI (Cordier et al. 2007) isochrones for $[\mathrm{M/H}] = -0.35$ ($Z_\mathrm{i} = 0.008$); (b) Padova (Marigo et al. 2008) for $[\mathrm{M/H}] = -0.375$ ($Z_\mathrm{i} = 0.008$); (c) MIST (Choi et al. 2016) for $[\mathrm{M/H}] = -0.37$ ($Z_\mathrm{i} = 0.006$); (d): `PARSEC-COLIBRI` isochrones (this work) for $[\mathrm{M/H}] = -0.37$ ($Z_\mathrm{i} = 0.006$). The heavy lines are for $n_\mathrm{inTPC} = 0$; the light ones are for $n_\mathrm{inTPC} = 25$.

$N^j(t)$ caused by the AGB-boosting period is of about $\Delta \log t \simeq 0.005$ dex. Since this parameter can be set to any arbitrarily small number, we recommend the galaxy-modeling community to use even finer resolutions in the vicinity of $\log(t/\mathrm{yr}) \simeq 9.2$, so that the spike in the TP-AGB star numbers associated with the AGB-boosting effect can be detected and well sampled, and eventually distributed over the age bin considered in the modeling of galaxies.

3.8. Comparison with Other Isochrones

Owing to the numerical complexity and sizeable uncertainties in the evolution of TP-AGB stars, isochrones including this phase are still rare. Moreover, the few available sets of such isochrones are far from being similar—as frequently occurs instead for evolutionary stages like the main sequence, RGB, or CHeB. Figure 11 presents a chronological sequence of such isochrones, zooming on the TP-AGB region of the HRD. The comparison is made for metallicity values comparable to that of young populations in the LMC, namely $[\mathrm{M/H}] = -0.35$ dex, which translates in slightly different values of Z_i in the different sets, depending on their definition of their solar value. A few differences are well evident in the figure:

1. The Cordier et al. (2007) isochrones, which have extended the BaSTI database with the complete TP-AGB evolution, actually miss a lot of its details. The most evident difference the lack of a transition to the C-star phase in these isochrones. Moreover the slope of their TP-AGB sequences in the HRD is clearly different from the pre-AGB evolution. This is certainly due to the very basic synthetic TP-AGB modeling—entirely based on fitting relations rather on envelope integrations—they have adopted. Also the old Padova isochrones from Girardi et al. (2000) present a similar level of simplicity in their TP-AGB sections.
2. As already mentioned, the work by Marigo et al. (2008) represented a major effort to include detailed TP-AGB sections in isochrones. At first glance, their isochrones appear similar to present ones with $n_\mathrm{inTPC} = 0$. However, there are many different details, like for instance the nearly absence of "glitches" in the present tables, due to the larger grids of tracks and improved interpolation schemes; the shorter extension in T_eff due to the more accurate low-temperature opacities; and the different extensions to high luminosities in the younger

isochrones, due to a more detailed treatment of HBB and mass loss. Moreover, there are subtle differences in the distribution of stars along these isochrones that do not appear in this particular figure; they have been discussed by Marigo et al. (2013), Rosenfield et al. (2014, 2016), and will not be repeated here. We also remark that similar TP-AGB sections are also found in the Bertelli et al. (2008, 2009) sets of isochrones.

3. The recent MIST isochrones (Choi et al. 2016) include the TP-AGB phase computed with a full evolutionary code, together with its L–$T_{\rm eff}$ variations due to TPCs. Their isochrone sequences appear more irregular than ours, owing to their more direct interpolation between TP-AGB tracks (see Dotter 2016). This aspect, however, should be seen as a less important—and mostly aesthetic—difference. The more important differences, instead, are in their C-star sections, which clearly start at a later point along the TP-AGB than ours, and for a decisively shorter age range. These features are very likely another manifestation of the old "C-star mystery" (see Iben 1981; Lattanzio & Wood 2004; Herwig 2005), found in stellar evolution models that apply standard methods to model the extent of third dredge-up events. Moreover, the C-rich sequences in MIST are in general hotter than in our isochrones, as a result of their use of molecular opacities derived for O-rich mixtures.

Apart from the differences in the HRD, there will be other significant ones in diagrams relating other variables, such as the $M_{\rm i}$, which determines the occupation probability of every isochrone section.

4. CONCLUDING REMARKS

As thoroughly discussed in Marigo et al. (2013) and Rosenfield et al. (2016), the COLIBRI code models third dredge-up and mass loss via a few simplified prescriptions. They contain parameters which, although reasonably constrained, have to be fine-tuned so as to reproduce the properties of TP-AGB star samples in nearby star clusters and galaxies, over the widest possible range of ages and metallicities. Moreover, all the grids of theoretical models involved in the construction of these isochrones are being expanded. This implies that present models will be frequently revised, in the context of the ERC-funded project STARKEY to calibrate the TP-AGB phase. Therefore, the present paper presents just a first snapshot of the isochrones involved in this process.

Isochrones presented in this paper, and in subsequent releases, can be retrieved from both the traditional CMD site (http://stev.oapd.inaf.it/cmd) and from the new web server (http://starkey.astro.unipd.it/cgi-bin/cmd). The servers provide isochrones computed on the fly, within seconds, for any sequence of ages and metallicities, and for a large set of predefined photometric systems. Additional computations—like luminosity functions and integrated magnitudes of stellar populations in several passbands—are also possible. Additional filters can be added upon request.

We note that massive stars/young isochrones are provided by the web interface as well, even if they do not regard the TP-AGB phase. Such massive star models are described in Tang et al. (2014) and Chen et al. (2015), to whom we refer for all details.

The same isochrones are also being implemented as new alternatives in the TRILEGAL (Girardi et al. 2005) code for simulating the photometry of resolved stellar populations, and in the PARAM code (da Silva et al. 2006; Rodrigues et al. 2014) for the Bayesian estimation of the properties of observed stars.

We acknowledge the support from the ERC Consolidator Grant funding scheme (*project STARKEY*, G.A. n. 615604). L.G. and T.S.R. acknowledge partial support from PRIN INAF 2014—CRA 1.05.01.94.05.

REFERENCES

Allard, F., Homeier, D., & Freytag, B. 2012, RSPTA, 370, 2765
Aringer, B., Girardi, L., Nowotny, W., Marigo, P., & Bressan, A. 2016, MNRAS, 457, 3611
Aringer, B., Girardi, L., Nowotny, W., Marigo, P., & Lederer, M. T. 2009, A&A, 503, 913
Bertelli, G., Bressan, A., Chiosi, C., Fagotto, F., & Nasi, E. 1994, A&AS, 106, 275
Bertelli, G., Girardi, L., Marigo, P., & Nasi, E. 2008, A&A, 484, 815
Bertelli, G., Nasi, E., Girardi, L., & Marigo, P. 2009, A&A, 508, 355
Boothroyd, A. I., & Sackmann, I.-J. 1988, ApJ, 328, 632
Boyer, M. L., Girardi, L., Marigo, P., et al. 2013, ApJ, 774, 83
Boyer, M. L., Srinivasan, S., van Loon, J. T., et al. 2011, AJ, 142, 103
Boyer, M. L., van Loon, J. T., McDonald, I., et al. 2010, ApJL, 711, L99
Bressan, A., Granato, G. L., & Silva, L. 1998, A&A, 332, 135
Bressan, A., Marigo, P., Girardi, L., et al. 2012, MNRAS, 427, 127
Bressan, A., Marigo, P., Girardi, L., Nanni, A., & Rubele, S. 2013, in 40th Liège Int. Astrophysical Colloq., Ageing Low Mass Stars: From Red Giants to White Dwarfs, ed. J. Montalbán, A. Noels, & V. Van Grootel (London: EDP Sciences), 03001
Caffau, E., Ludwig, H.-G., Steffen, M., Freytag, B., & Bonifacio, P. 2011, SoPh, 268, 255
Cardelli, J. A., Clayton, G. C., & Mathis, J. S. 1989, ApJ, 345, 245
Castelli, F., & Kurucz, R. L. 2003, in IAU Symp. 210, Modelling of Stellar Atmospheres, ed. N. Piskunov, W. W. Weiss, & D. F. Gray (Cambridge: Cambridge Univ. Press), A20
Chaplin, W. J., & Miglio, A. 2013, ARA&A, 51, 353
Charlot, S., & Bruzual, A. G. 1991, ApJ, 367, 126
Chen, Y., Bressan, A., Girardi, L., et al. 2015, MNRAS, 452, 1068
Chen, Y., Girardi, L., Bressan, A., et al. 2014, MNRAS, 444, 2525
Choi, J., Dotter, A., Conroy, C., et al. 2016, ApJ, 823, 102
Cioni, M.-R., Loup, C., Habing, H. J., et al. 2000, A&AS, 144, 235
Cordier, D., Pietrinferni, A., Cassisi, S., & Salaris, M. 2007, AJ, 133, 468
da Silva, L., Girardi, L., Pasquini, L., et al. 2006, A&A, 458, 609
Demarque, P., & McClure, R. D. 1977, ApJ, 213, 716
Dolphin, A. E. 2002, MNRAS, 332, 91
Dotter, A. 2016, ApJS, 222, 8
Eriksson, K., Nowotny, W., Höfner, S., Aringer, B., & Wachter, A. 2014, A&A, 566, A95
Fluks, M. A., Plez, B., The, P. S., et al. 1994, A&AS, 105, 311
Fox, M. W., & Wood, P. R. 1982, ApJ, 259, 198
Frogel, J. A., Mould, J., & Blanco, V. M. 1990, ApJ, 352, 96
Frost, C. A., & Lattanzio, J. C. 1996, ApJ, 473, 383
Gail, H.-P., & Sedlmayr, E. 1998, FaDi, 109, 303
Girardi, L., & Bertelli, G. 1998, MNRAS, 300, 533
Girardi, L., Bertelli, G., Bressan, A., et al. 2002, A&A, 391, 195
Girardi, L., Bressan, A., Bertelli, G., & Chiosi, C. 2000, A&AS, 141, 371
Girardi, L., Groenewegen, M. A. T., Hatziminaoglou, E., & da Costa, L. 2005, A&A, 436, 895
Girardi, L., & Marigo, P. 2007, in ASP Conf. Ser. 378, Why Galaxies Care About AGB Stars: Their Importance as Actors and Probes, ed. F. Kerschbaum, C. Charbonnel, & R. F. Wing (San Francisco, CA: ASP), 20
Girardi, L., Marigo, P., Bressan, A., & Rosenfield, P. 2013, ApJ, 777, 142
Girardi, L., Williams, B. F., Gilbert, K. M., et al. 2010, ApJ, 724, 1030
Glatt, K., Gallagher, J. S., III, Grebel, E. K., et al. 2008b, AJ, 135, 1106
Glatt, K., Grebel, E. K., Sabbi, E., et al. 2008a, AJ, 136, 1703
Groenewegen, M. A. T. 2006, A&A, 448, 181
Groenewegen, M. A. T. 2012a, A&A, 543, A36
Groenewegen, M. A. T. 2012b, A&A, 540, A32
Herwig, F. 2005, ARA&A, 43, 435
Iben, I., Jr. 1981, ApJ, 246, 278

Ivezic, Z., & Elitzur, M. 1997, MNRAS, 287, 799
Jager, C., Mutschke, H., & Henning, T. 1998, A&A, 332, 291
Komatsu, E., Smith, K. M., Dunkley, J., et al. 2011, ApJS, 192, 18
Kroupa, P. 2002, Sci, 295, 82
Lattanzio, J. C., & Wood, P. R. 2004, in Asymptotic Giant Branch Stars, ed. H. J. Habing & H. Olofsson (New York: Springer), 23
Loidl, R., Lançon, A., & Jørgensen, U. G. 2001, A&A, 371, 1065
Marigo, P. 2002, A&A, 387, 507
Marigo, P. 2015, ASP Conf. Ser. 497, Why Galaxies Care about AGB Stars III: A Closer Look in Space and Time, ed. F. Kerschbaum, R. F. Wing, & J. Hron (San Francisco, CA: ASP), 229
Marigo, P., & Aringer, B. 2009, A&A, 508, 1539
Marigo, P., Bressan, A., Nanni, A., Girardi, L., & Pumo, M. L. 2013, MNRAS, 434, 488
Marigo, P., & Girardi, L. 2007, A&A, 469, 239
Marigo, P., Girardi, L., Bressan, A., et al. 2008, A&A, 482, 883
Marigo, P., Girardi, L., & Chiosi, C. 2003, A&A, 403, 225
Martig, M., Fouesneau, M., Rix, H.-W., et al. 2016, MNRAS, 456, 3655
Masseron, T., & Gilmore, G. 2015, MNRAS, 453, 1855
Miglio, A., Brogaard, K., Stello, D., et al. 2012, MNRAS, 419, 2077
Momany, Y., Saviane, I., Smette, A., et al. 2012, A&A, 537, A2
Mowlavi, N. 1999, A&A, 344, 617
Mucciarelli, A., Origlia, L., & Ferraro, F. R. 2007, AJ, 134, 1813
Nanni, A., Bressan, A., Marigo, P., & Girardi, L. 2013, MNRAS, 434, 2390
Nanni, A., Bressan, A., Marigo, P., & Girardi, L. 2014, MNRAS, 438, 2328
Nanni, A., Marigo, P., Groenewegen, M. A. T., et al. 2016, MNRAS, 462, 1215
Ness, M., Hogg, D. W., Rix, H.-W., et al. 2016, ApJ, 823, 114
Nikolaev, S., & Weinberg, M. D. 2000, ApJ, 542, 804
O'Donnell, J. E. 1994, ApJ, 422, 158
Ostlie, D. A., & Cox, A. N. 1986, ApJ, 311, 864
Paczynski, B. 1996, ARA&A, 34, 419
Reimers, D. 1975, MSRSL, 8, 369
Rodrigues, T. S., Girardi, L., Miglio, A., et al. 2014, MNRAS, 445, 2758
Rosenfield, P., Marigo, P., Girardi, L., et al. 2014, ApJ, 790, 22
Rosenfield, P., Marigo, P., Girardi, L., et al. 2016, ApJ, 822, 73
Rouleau, F., & Martin, P. G. 1991, ApJ, 377, 526
Salaris, M., Pietrinferni, A., Piersimoni, A. M., & Cassisi, S. 2015, A&A, 583, A87
Seaton, M. J. 2005, MNRAS, 362, L1
Skrutskie, M. F., Cutri, R. M., Stiening, R., et al. 2006, AJ, 131, 1163
Tanabé, T., Kučinskas, A., Nakada, Y., Onaka, T., & Sauvage, M. 2004, ApJS, 155, 401
Tang, J., Bressan, A., Rosenfield, P., et al. 2014, MNRAS, 445, 4287
van der Marel, R. P., & Cioni, M.-R. L. 2001, AJ, 122, 1807
van Loon, J. T., Marshall, J. R., & Zijlstra, A. A. 2005, A&A, 442, 597
Vassiliadis, E., & Wood, P. R. 1993, ApJ, 413, 641
Wagenhuber, J. 1996, PhD thesis, Techn. Univ. München
Wagenhuber, J., & Groenewegen, M. A. T. 1998, A&A, 340, 183
Wood, P. R. 2015, MNRAS, 448, 3829
Wood, P. R., Bessell, M. S., & Fox, M. W. 1983, ApJ, 272, 99
Wood, P. R., & Olivier, E. A. 2014, MNRAS, 440, 2576
York, D. G., Adelman, J., Anderson, J. E., Jr., et al. 2000, AJ, 120, 1579